



저작자표시-비영리-변경금지 2.0 대한민국

이용자는 아래의 조건을 따르는 경우에 한하여 자유롭게

- 이 저작물을 복제, 배포, 전송, 전시, 공연 및 방송할 수 있습니다.

다음과 같은 조건을 따라야 합니다:



저작자표시. 귀하는 원저작자를 표시하여야 합니다.



비영리. 귀하는 이 저작물을 영리 목적으로 이용할 수 없습니다.



변경금지. 귀하는 이 저작물을 개작, 변형 또는 가공할 수 없습니다.

- 귀하는, 이 저작물의 재이용이나 배포의 경우, 이 저작물에 적용된 이용허락조건을 명확하게 나타내어야 합니다.
- 저작권자로부터 별도의 허가를 받으면 이러한 조건들은 적용되지 않습니다.

저작권법에 따른 이용자의 권리는 위의 내용에 의하여 영향을 받지 않습니다.

이것은 [이용허락규약\(Legal Code\)](#)을 이해하기 쉽게 요약한 것입니다.

[Disclaimer](#)

Ph.D. Dissertation

**Disposable MEMS optrode array for
multi-wavelength neurostimulation**

다파장 신경 자극을 위한 일회용 MEMS
광 탐침 어레이

February 2017

Seoul National University

Department of Electrical Engineering and Computer Science

Sunghyun Yoo

Ph.D. Dissertation

**Disposable MEMS optrode array for
multi-wavelength neurostimulation**

다파장 신경 자극을 위한 일회용 MEMS
광 탐침 어레이

February 2017

Seoul National University

Department of Electrical Engineering and Computer Science

Sunghyun Yoo

Disposable MEMS optrode array for multi-wavelength neurostimulation

다파장 신경 자극을 위한 일회용 MEMS
광 탐침 어레이

지도 교수 김 용 권

이 논문을 공학박사 학위논문으로 제출함
2017 년 2 월

서울대학교 대학원
전기·컴퓨터 공학부
유 승 현

유승현의 공학박사 학위논문을 인준함
2017 년 2 월

위 원 장	<u>전 국 진</u>	(인)
부위원장	<u>김 용 권</u>	(인)
위 원	<u>박 남 규</u>	(인)
위 원	<u>김 호 성</u>	(인)
위 원	<u>지 창 현</u>	(인)

Abstract

This dissertation presents an optical neural probe for an implantable multi-wavelength photostimulation system based on a newly-proposed MEMS optrode array (MOA) with improved light delivery efficiency and capability. The proposed system delivered the highest total light power from a single commercially available LED to the distal tip of the waveguide among conventional LED-waveguide-based optical neural probes by expanding the waveguide into an array. To improve light delivery, a novel MEMS microlens array was adopted as the optical collimator between the light source and the waveguide. This research also proposes and validates a simple and practical method for suppressing surface crystallization of borosilicate glass during high temperature annealing as well as a method of modeling and fabricating a through-substrate square-shaped glass microlens array using thermal reflow process, both for the first time in this field of research.

The probe proposed in this study comprises of a disposable MOA and a reusable unit, where the MOA is fabricated by manually assembling a 4×4 array of 6 mm-long optical fibers with a 4×4 array of thermally-reflowed square-shaped glass microlenses. The reusable unit includes a domed-top LED and driving circuitry. The MOA, developed for implantation on a nerve system, is separable from the LED light source to reduce the risk of infection from probe reuse while minimizing the waste of the probe after animal experiments. The optimal geometry of the microlens was derived through finite element analysis on computational fluid dynamics and geometrical optics.

Surface crystallization on borosilicate glass, which is a well-known and fatal limitation that can occur when fabricating a three-dimensional glass structure via thermal reflow process, was effectively prevented on a commercially available glass wafer by applying a simple surface treatment prior to the annealing. Quantitative analysis of the crystallization and surface ion concentration verified that 30 seconds or more of fluorine plasma treatment can significantly suppress the nucleation of cristobalites. Average surface roughness and optical transparency were enhanced 15 times and 3 times, respectively, compared to untreated samples, suggesting that the proposed method is practical for vitrification in borosilicate glass during the thermal reflow process.

Square-shaped glass microlenses with a footprint of $300 \times 300 \mu\text{m}^2$ were uniformly fabricated in good agreement with the finite analysis modeling. Vitrified surfaces with an average surface roughness of 47 nm was achieved through the proposed procedure. The measurement results fully validated the fabrication procedure and the capability of the microlens array as light collimating optics in the proposed neural probe. The fabrication of the MEMS optrode array including fiber manipulation and assembly was carried out with customized aid apparatus. Optical characterization of the MEMS optrode array is presented, followed by an analysis of loss factors. The capabilities and limitations of the present device is discussed in terms of the multi-wavelength illumination and disposable functionality.

The total light delivery efficiency of the probe was measured to be -10.63 dB, of which the use of microlenses attributed to the improvement of 3.15 dB. Light loss was mainly caused by the coupling loss between the LED and the microlens, which is estimated to be -6.04 dB, and the rough facets of the diced optical fibers. A more

precise and robust design for the assembly sheath will be also helpful in significantly preventing the degradation of light delivery efficiency caused by misalignment between the disposable MOA and the reusable LED unit.

Keywords: Neural probe, MEMS optrode array, light delivery efficiency, glass microlens, thermal reflow process, surface crystallization

Student number: 2012-30940

Table of contents

Abstract	i
Table of contents	iv
List of tables	vii
List of figures	vii
1. Introduction.....	1
1.1 Optogenetics.....	1
1.2 Optical neural interface	5
1.3 Literature review: LED-based light delivery probe	10
1.3.1 LED-based light delivery	10
1.3.2 Reliability and biocompatibility	14
1.3.3 Multi-wavelength illumination.....	15
1.3.4 Summary	17
1.4 Research objectives.....	19
1.5 Originality and contribution.....	21
2. Light delivery probe with MEMS optrode array	22
2.1 Introduction	22
2.2 Proposal and overall design.....	23
2.3 Theoretical light delivery	26
2.3.1 Theoretically achievable maximum efficiency	26
2.3.2 Fresnel reflection.....	27
2.3.3 Coupling efficiency	29
2.4 Computational design of thermally reflowed square-shaped microlens ..	32

2.5 Conclusion.....	36
3. Suppression of surface crystallization on borosilicate glass	37
3.1 Introduction.....	37
3.1.1 Surface crystallization	37
3.1.2 Literature review: suppression of glass crystallization	39
3.2 Proposal and method.....	41
3.3 Results and discussion.....	44
3.3.1 Suppression of surface crystallization.....	44
3.3.2 Surface ion concentrations and roughness	47
3.3.3 Surface characterization	49
3.4 Conclusion.....	54
4. Through-substrate square-shaped glass microlens array	55
4.1 Introduction.....	55
4.1.1 MEMS microlens and microlens array.....	55
4.1.2 Monolithically integrated glass microlens	57
4.2 Microfabrication procedure.....	63
4.3 Results and discussion.....	65
4.3.1 Fabrication results	65
4.3.2 Surface profile and roughness	67
4.3.3 Influence of oxygen plasma on crystallization.....	69
4.4 Conclusion.....	71
5. MEMS optrode array: fabrication and characterization	72
5.1 Introduction.....	72
5.2 Fiber manipulation and assembly.....	73
5.2.1 Optical fiber preparation	73
5.2.2 Fiber assembly.....	75
5.3 Optical characterization.....	78
5.3.1 Measurement setup.....	78
5.3.2 Light delivery efficiency	78

5.3.3 Loss factor analysis	80
5.4 Capability and limitation	84
5.4.1 Disposable configuration.....	84
5.4.2 Multi-wavelength illumination.....	85
5.5 Conclusion.....	89
6. Conclusion	92
Bibliography.....	94
Abstract (Korean).....	103

List of tables

Table 2.1. Refractive index of substances.	28
Table 2.2. Reflectance and transmittance at various interfaces.....	29
Table 2.3. Estimated light delivery efficiency of the proposed neural probe.....	36
Table 5.1. Summary of the measured light delivery efficiency.....	89
Table 5.2. Light delivery efficiency of LED-waveguide-based neural probes.....	90

List of figures

Figure 1.1. Fundamental procedure of neurostimulation in optogenetics	2
Figure 1.2. (a) Comparison between optical and electrical stimulation and (b) various types of light-gated ion channels, opsins.....	3
Figure 1.3. Optical fiber as a light delivering probe in the initial stages	6
Figure 1.4. Various optical neural interfaces utilizing laser light sources	7
Figure 1.5. Light attenuation as a function of penetration depth in a typical tissue	11
Figure 1.6. Light output power of neural probes used in living animal experiment	12
Figure 1.7. Comparison of power efficiency within LED-based neural probes.....	13
Figure 1.8. LED-based optical neural interfaces.....	17
Figure 2.1. Schematic diagram of the proposed light delivering probe.	24
Figure 2.2. Fresnel reflections in the MEMS optrode array.....	27

Figure 2.3. Light coupling loss in the MEMS optrode array	30
Figure 2.4. Comparison of the effective light receiving area of the microlens arranged in array.....	33
Figure 2.5. FEM simulation results.....	34
Figure 3.1. Schematic diagram of sample preparation procedure	42
Figure 3.2. Optical images of BSG surface after the 3 hours of thermal reflow process at 850 °C.....	45
Figure 3.3. The number of formed cristobalites on BSG surface as a function of plasma treatment period.	47
Figure 3.4. X-ray photoemission spectroscopy results. Surface ion concentration as a function of the plasma treatment time.	48
Figure 3.5. SEM image of the cristobalites and induced micro-cracks on reflowed glass surface.	50
Figure 3.6. SEM images of the reflowed glass surfaces.	51
Figure 3.7. Measured surface profile within area of 1.6x1.6 mm ² at the center part of the glass samples using confocal-based 3D surface profiler.	52
Figure 3.8. Optical transparency measurement.	53
Figure 4.1. Monolithically integrated glass microlens	57
Figure 4.2. Fabrication process of the pre-assembled microlens	59
Figure 4.3. Schematic diagram of the spherical microlens before and after the thermal reflow process	60
Figure 4.4. SEM images of the fabricated glass cylinder (a) and the reflowed microlens (b)	61
Figure 4.5. Surface profile comparison of the calculated and measured profile of the spherical microlens.....	62
Figure 4.6. Microfabrication procedure of the square-shaped glass microlens array	

with fiber guiding structure	63
Figure 4.7. Fabrication result of square-shaped glass microlens array	65
Figure 4.8. Comparison of glass leveling results between with and without plasma treatment prior to the anodic bonding	67
Figure 4.9. Surface profile measurement of the square-shaped glass microlens.....	68
Figure 4.10. Influence of oxygen plasma on surface crystallization of borosilicate glass.....	70
Figure 5.1. Optical image of silicon v-groove substrate for fiber segmentation.	74
Figure 5.2. Microscopic images of facets of the segmented optical fiber using silicon v-grooves and dicing saw.....	75
Figure 5.3. Microscopic image of the through-Si jig (a) and optical image of the micromachined aluminum aligner (b).	76
Figure 5.4. Optical image of the fabricated MEMS optrode array.	77
Figure 5.5. Light output power comparison between the LED and the fiber array.	79
Figure 5.6. Illustration of measurement condition for comparison of the light output power between with and without the microlens	81
Figure 5.7. Comparison of the measured light power between with and without the microlens array.....	81
Figure 5.8. Illustration of measurement condition for comparison of the light output power between with and without the aperture.....	82
Figure 5.9. Practical light power transmitted to the area of light receiving region of the microlens array	83
Figure 5.10. Optical images of (a) the fabricated MEMS optrode array, (b) domed-top LED with LED driver, and (c) the overall device including the MEMS optrode array and the reusable unit.....	84
Figure 5.11. Light power measurement.....	85

Figure 5.12. Optical image of the multi-wavelength illumination test.....	86
Figure 5.13. Light delivery efficiency of the blue light	87
Figure 5.14. Light delivery efficiency of the yellow light	88
Figure 5.15. Comparison of power efficiency between the proposed neural probe and conventional LED-based neural probes.....	91

1. Introduction

1.1 Optogenetics

Optogenetics is a field of research that studies the controlling and probing of neural activities using light stimulation [1, 2] which gained momentum in the early 2000s [3]. Due to its unique and powerful characteristics such as cell-type selectivity and biosafety, optogenetics has gained increasing interest as a potential solution for human neurological diseases, with its application expanding to a greater diversity of areas, e.g. clinical treatment for blindness and controlling cellular functions of plants [4].

In general, the experimental procedure in optogenetics consists of two primary steps, *genetic manipulation* and *optical control and probing*, as depicted in detail in Figure 1.1 [5]. In the first step, genetic manipulation, a gene is attached with a promoter then inserted into a virus. Then, the transgenic virus is injected into a target area in a nerve system, such as a mammalian brain. Within a couple of weeks, the virus infects many nerve cells in the area, during which only the targeted neurons that are specified by the promoter produce opsin proteins.

Opsin is a light-sensitive protein that plays a central role in optogenetics [6]. Through the procedure described above, the targeted neurons are genetically manipulated to produce opsins, which function as light-gated ion channels as illustrated in Figure 1.2(b) [7].

Making Neurons React to Light

For optogenetic studies, neuroscientists insert opsin genes into brain cells with the aid of engineered viruses. They can then trigger neural activity on demand with flashes of light and observe the effects on experimental animals' behavior.

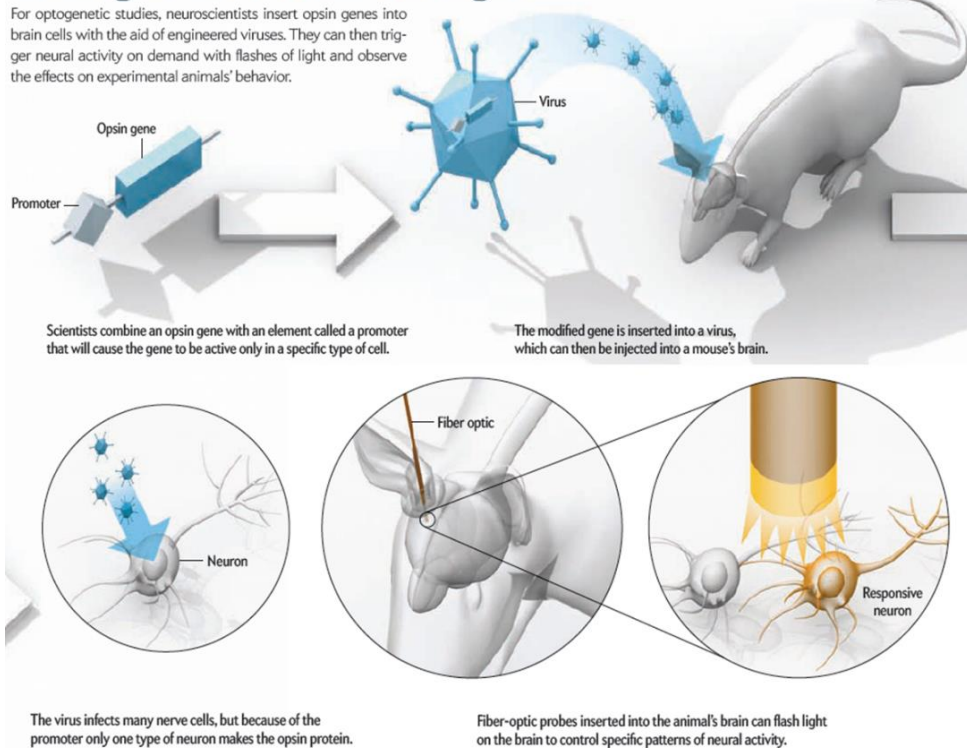


Figure 1.1. Fundamental procedure of neurostimulation in optogenetics [5]

In the second step, optical control and probing, a light delivery probe is inserted into the brain and light is flashed on the neural cells, which renders response from only the targeted neurons. The result of the photostimulation is analyzed by either observing the animal behavior or measuring the electrical potential variation near the neural cell.

The advantage of optogenetics becomes clear when compared to conventional electrical stimulation and probing. In general, electrical stimulation involves inserting an electrode inside the body and applying voltage on the electrode. A separate sensing electrode is inserted in the close periphery of the stimulating

biosafety, nevertheless, this approach is fundamentally vulnerable to risks involving local high current density and electrical leakage.

1.2 Optical neural interface

Researches on optogenetics so far can be categorized into two main branches: the development of opsin genes including transgenic technology [6] and the development of optical neural interfaces [7]. Progress in either branch to improve the opsin or the control interfaces can extend the scope and applications of experiments to contribute greatly in mending the gap in the human knowledge of the neural system.

Optical neural interface is a miniaturized device that delivers light into the targeted area of the neural system as its basic function. The past decade has seen significant progress in these elaborate devices, including integration of multiple sensing electrodes, microfluidic channels for drug injection, and temperature monitoring sensors. The interfaces can be grouped into two major types by the light source they use: laser-based [8-14] and light emitting diode (LED)-based [15-21].

In the initial stages of development, optical fibers with external laser sources were the principal drivers of light delivery on targeted neural cells. A bare optical fiber was directly utilized as the light delivering probe for the first time in an experiment conducted by Dr. Deisseroth and his group at Stanford University on a living rodent [8, 9], which is illustrated in Figure 1.3 [9].

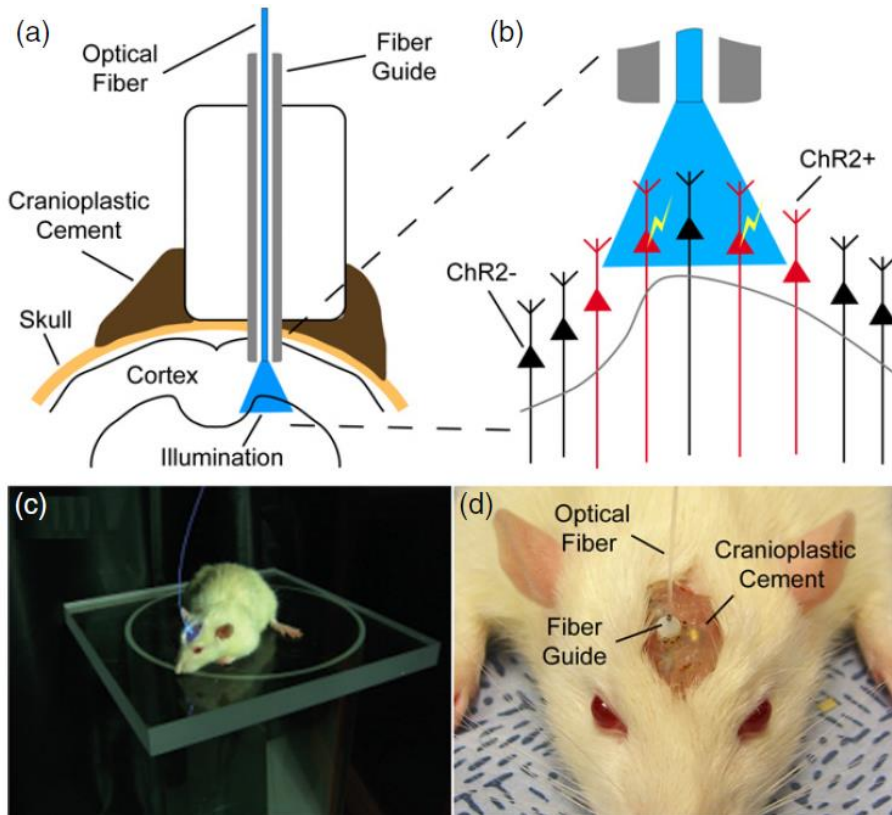


Figure 1.3. Optical fiber as a light delivering probe in the initial stages [9]

Laser light sources have many advantages over other candidates, such as high output light intensity, low light beam divergence, and coherence with narrow bandwidth. Direct illumination via optical fiber inherits the optical advantages of fiber-optic and laser-based systems while adding low light loss performance to the list of merits mentioned above. This approach also benefits from various mature peripheral equipment technologies used in the field of fiber optics. Moreover, compared with other types of approaches, configurations using bare optical fiber allow more scalability in probe length, which is critical in deep brain stimulation. Later, laser-based optical fibers were integrated with metal electrodes [10, 11],

polymer-based waveguides [12, 13], and glass optrode array [14] by different research groups. The examples of optical neural interfaces utilizing laser light sources are summarized in Figure 1.4 [22].

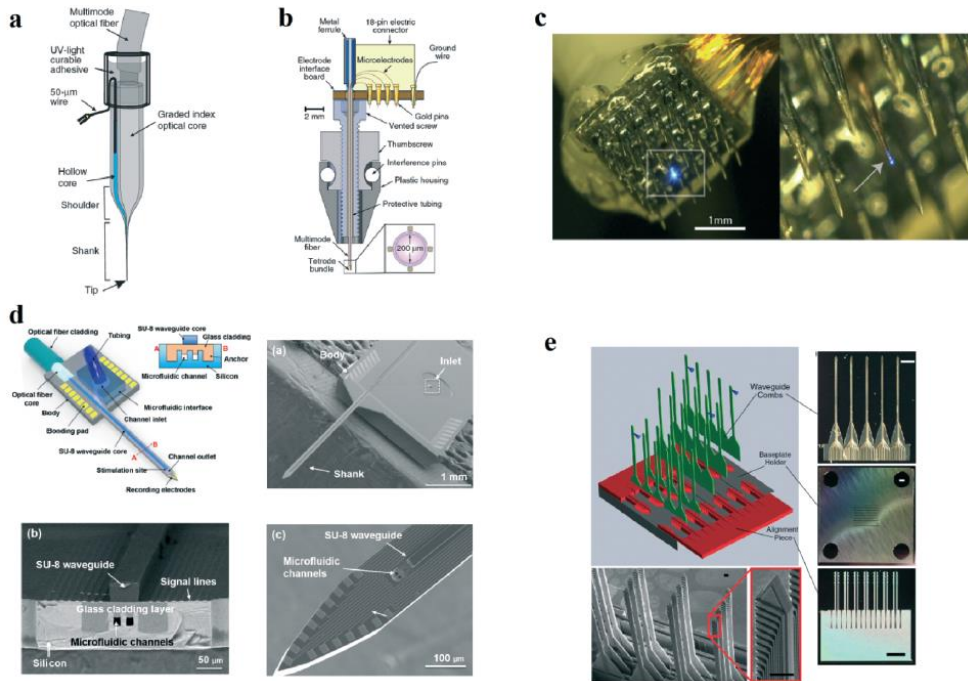


Figure 1.4. Various optical neural interfaces utilizing laser light sources [22]

Despite the numerous merits mentioned above, however, conventional fiber-based configuration with a laser source has several fundamental limitations. First, it is hard to implement as an untethered wireless control system due to the mechanical stiffness of optical fiber connections. This constraint becomes worse when the light probe is either extended to an array, which is a bundle of fibers, or integrated with additional electrical electrodes for read out. The limited scalability of the array and low spatial resolution of the fibers are also matters that need to be addressed in these

types of fiber-optic probe, considering that fibers need to be glued and fixed to the bulky guide structure.

Contrary to laser and laser diode, LED can be relatively preferable considering the recent demands on optical neural interface. Recently, studies have reported successful integration of micro LEDs (μ LEDs), which are LEDs of sizes ranging from tens to hundreds of micrometers, on the light delivering probe by microfabrication [15, 23]. There are also commercially available products that come in various specifications in terms of size, wavelength, output power, and configuration [24-26]. LEDs come in small sizes with high spatial resolution and low power consumption which are vital properties for implementing a wirelessly controlled system. In addition, their stable illumination and fast switching speed also make LEDs suitable for the system.

However, due to the incoherent and Lambertian light emission of LEDs, LED-based probes fundamentally suffer from low light coupling efficiency between the light source and the waveguide, which also causes light power handling issues. On the other hand, direct cell illumination from μ LEDs has more efficient light emission than illumination through waveguides, however, considerable concerns are being voiced about the reliability and biocompatibility of this type of configuration due to the high amount of localized current and heat that occur.

Incidentally, significant research has been conducted on both laser-based and LED-based optical neural interfaces to add greater functionality including bi-directionality, multi-wavelength illumination, drug delivery, integration of various sensors.

In the following chapter, a detailed literature review on LED-based light

delivering probe will be provided under the three sub-themes listed below, based on the challenges that remain to be tackled in this field of research [4, 7, 22].

- Efficient light delivery for neurostimulation
- Reliability and biocompatibility
- Multi-wavelength illumination

1.3 Literature review: LED-based light delivery probe

1.3.1 LED-based light delivery

Efficient delivery of sufficient light power is one of the most important and fundamental requirements of optical neural interfaces. Effective light delivery becomes more crucial when the probes are designed for a wireless control system with limited electricity, which is becoming more common in recent years.

The light intensity required for the activation of light-sensitive opsins are well known to be $>1\text{-}5\text{ mW/mm}^2$ of blue light for *in vitro* stimulation [27, 28] and $>7\text{ mW/mm}^2$ for *in vivo* inhibition when measured with red light [29]. However, simply assuring enough light intensity is often not enough in practice due to a couple of undesired optical phenomena, that is, light absorption and scattering in tissue.

Light intensity exponentially attenuates as a function of penetration depth, and as shown in Figure 1.5 [8], it has been reported that the irradiance decreases to below 10%, as compared to tissue surface, within about $300\text{ }\mu\text{m}$ depth [8, 30]. Therefore, practical *in vivo* photostimulation on living animals requires a much higher grade of light power at the probe tip. Alternatively, an accurate insertion that puts the probe facet close to the targeted area in terms of insertion depth can minimize the required light output power.

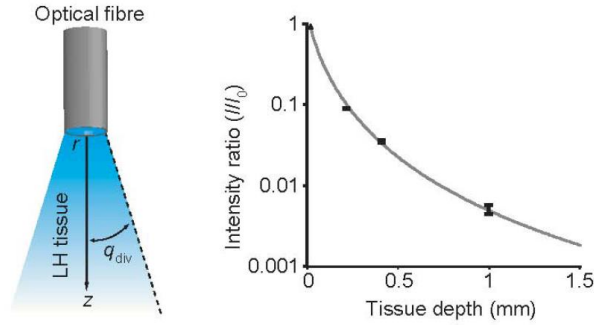


Figure 1.5. Light attenuation as a function of penetration depth in a typical tissue [8]

On the other hand, precise lateral alignment between the probe and the targeted area can also affect the success or failure of sufficient light delivery during a practical animal experiment. Figure 1.6 plots the maximum instantaneous light intensity used in photostimulations on living animals as a function of the illumination area of the probe, from three laser-based [12, 13, 31] and six LED-based [15-20] neural probes. While the light intensity required for the activation of channelrhodopsin-2 (ChR2) is well known to be 1 mW/mm^2 [27, 28], practical intensities used in animal experiments are several orders higher, up to 1714 mW/mm^2 , at the probe tip. In the figure, the red line refers to the rational function with the average light output power (0.946 mW) as the coefficient of the function, and indicates that practical photostimulation requires a certain amount of total light power for its success. Furthermore, probes with small illumination areas require higher light intensity in practice than probes with large illumination areas, as probes with relatively small illuminations area are more vulnerable to lateral misalignment.

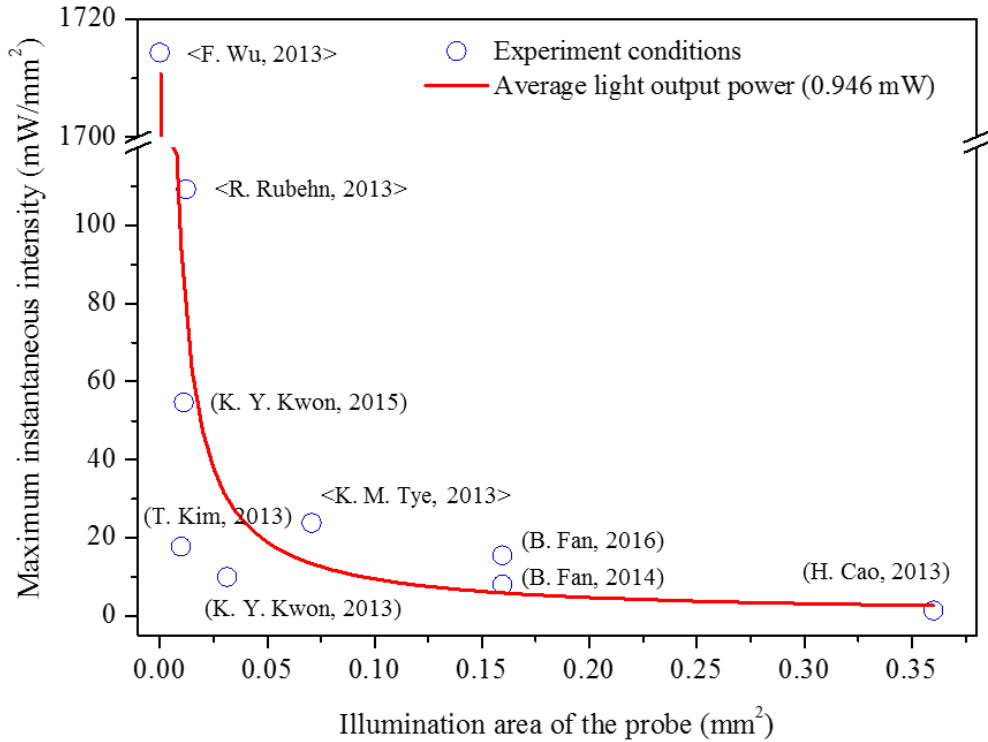
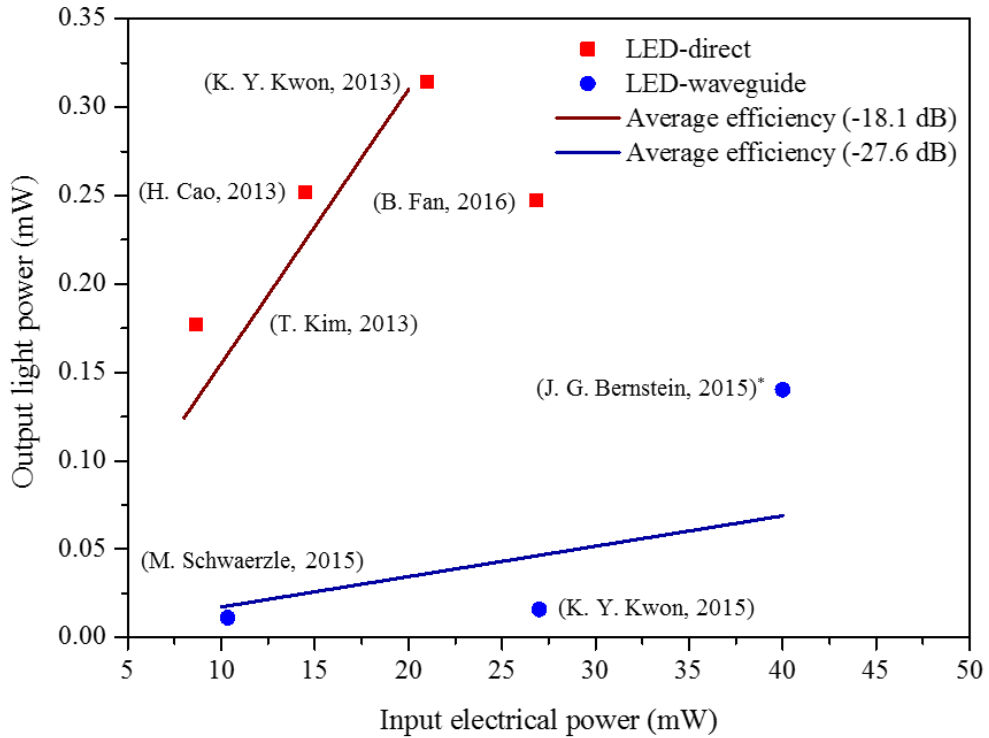


Figure 1.6. Light output power of neural probes used in living animal experiment

Despite the practical requirement of total light power for photostimulations on living animals, current LED-based neural probes with waveguides generally have low power coupling efficiency, which is the amount of light power delivered at probe tip as compared to the consumed electrical power. Figure 1.7 summarizes the power coupling efficiency of current LED-based neural probes [15-17, 19, 20, 32, 33]. It clearly verifies that probes with waveguides have much lower average power efficiency, at -27.6 dB. In this sense, LED-based probes with waveguides require a power-handling capability of 544 mW to achieve 0.946 mW output light power, which is barely suitable for wireless control systems, especially for biomedical application. On the other hand, LED-based probes without waveguides require only

61 mW for the same output light power. Due to the low light coupling efficiency between the LED and the waveguide, the direct utilization of LED is more competitive for a wirelessly controlled system.



*: Values were scaled down to 1/50 (actual input and output power are 2 W and 7 mW, respectively.)

Figure 1.7. Comparison of power efficiency within LED-based neural probes

1.3.2 Reliability and biocompatibility

Ensuring both reliability and biocompatibility are important requisites of neural interfaces for biomedical application. Many neural interfaces in optogenetics eventually aim to realize a wireless, implantable therapeutic device for human chronic diseases [4].

Many researchers have provided well-organized validation on safety matters in their devices, as probes are generally inserted inside the living body with direct contact to neural cells. Nevertheless, direct insertion of a μ LED into the brain still needs utmost care with regards to both localized heat dissipation and electrical leakage.

Several researches have suggested integrating either a polymer waveguide or optical fibers as possible solutions to the potential hazards [19, 24, 32, 33]. In terms of the material used in the device, polymers are not yet fully validated for its long-term biocompatibility, which can be significant in chronic applications. For example, there have been reports of light delivery degradation in polymer waveguides [18, 19].

Probes with optical fibers as a waveguide [24, 32, 33] are implemented by integrating a segmented optical fiber with a LED. Although not yet fully validated, existing studies have elaborated on the feasibility of a two-dimensional fiber array for wirelessly controllable system [32, 33], and wirelessly controlled illumination through a single ferruled fiber has also been successfully demonstrated [24]. Since the LED is significantly larger than the fiber in terms of light receiving or transmitting area in these approaches, a monolithic configuration is applied for the

fibers and the light source or the whole system in their devices to maximize the light coupling efficiency between the LED and the fiber by arranging them in direct contact [34] and to free them from the alignment error during the assembly.

However, this configuration results in a large amount of wasted parts after the biological experiment, with the costs exponentially increasing when the probes have either fibers and LEDs in array or additionally integrated structures for advanced functionality. As a possible solution, the probes can be reused after appropriate cleaning and sterilization. However, the sterilized probes will still bear possible risks of infection.

1.3.3 Multi-wavelength illumination

Ever since the first validation on a living animal [8], optical neural probes have been improved in various aspects, including bi-directionality, drug delivery, temperature sensors, and multi-wavelength illumination. Among these advances, multi-wavelength illumination is essential for simultaneous stimulation and inhibition, considering that opsins such as channelrhodopsin (ChR), halorhodopsin (HR) respond to lights of different wavelength.

Direct utilization of optical fiber and laser source allows for a relatively easy implementation of multi-wavelength illumination. One way to realize the system is simply using a 1:2 fiber coupler and two separate laser sources. However, laser sources, especially yellow light, can be costly, with their prices ranging from \$5,000 to 10,000.

On the other hand, several hurdles must be overcome for LED-based light delivery, in terms of probes both with and without the waveguides. In general, LED-based neural probes have issues such as low light coupling efficiency and low output light power. In this situation, implementing a multi-wavelength configuration such as placing separate LEDs of different colors will exacerbate the situation. This may be the reason why there have been no reports, as far as we know, on multi-wavelength LED-based light delivery probes with high-perfection.

One approach to achieve a multi-wavelength direct LED illumination system is to place separate LEDs on the substrate or the silicon-based tips. However, this type of arrangement fundamentally lacks precise alignment and consistent illumination on the same target area. Moreover, the extremely complicated and difficult fabrication procedure of installing multiple LEDs are frequently mentioned as its drawbacks.

Compared to direct illumination, probes with waveguides are even more vulnerable to light power handling issues. In addition, conventional approaches utilizing optical fibers as waveguides adopt the butting method to optimize the light coupling efficiency between the LED and the optical fiber. In this configuration, installing multiple LED sources in the system requires a novel approach to break through the constraints.

As described above, many areas still require development to implement multi-wavelength illumination in present LED-based neural interfaces.

1.3.4 Summary

LED-based optical neural interfaces can be classified into two representative types: direct μ LED illumination and probes with waveguides. Probes with waveguides employ either microfabricated polymer waveguides or waveguides that utilize commercially available optical fiber. Figure 1.8 summarizes LED-based optical neural interfaces in consideration of merits and current issues in the field of research.

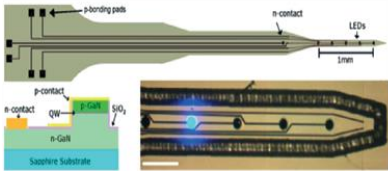
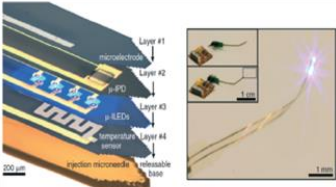
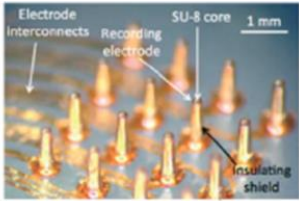
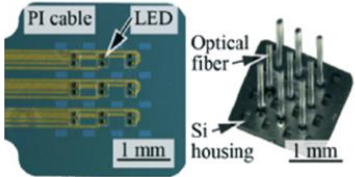
LED-based optical neural interface	
Without waveguides	<div style="display: flex; justify-content: space-around;"> <div style="text-align: center;">  <p>< N. McAlinden, 2013 ></p> </div> <div style="text-align: center;">  <p>< T. Kim, 2013 ></p> </div> </div>
With waveguides	<div style="display: flex; justify-content: space-around;"> <div style="text-align: center;">  <p>< K. Y. Kwon, 2015 ></p> </div> <div style="text-align: center;">  <p>< M. Schwaerzle, 2015 ></p> </div> </div>
Merits	<p>Wireless capability (Low power consumption, small size) / illumination stability / fast light-switching</p>
Issues	<p>Light power issue Low coupling efficiency, limited electricity</p> <p>Safety issues Thermal & electrical leakage (Direct contact with μLED), Material issues (Unverified polymers), Infection (reusing probes)</p>

Figure 1.8. LED-based optical neural interfaces

While the practical instantaneous light power required in the photostimulation is roughly 1 mW, current LED-based neural probes lack appropriate light power handling capability. In terms of sufficient light delivery, direct illumination using μ LEDs can be preferable for systems targeting wirelessly controlled, implantable devices. On the contrary, probes with waveguides can be more adequate for therapeutic usage, as this type of devices can achieve reliability and biocompatibility more easily due to being free from electrically and thermally induced risks.

In terms of the materials used in the devices, polymers have not yet been fully tested for their biosafety and reliable actuation. In this sense, utilizing commercially available optical fiber can be safer compared to polymer waveguides. However, utilizing optical fiber involves unavoidable manual and labor intensive procedures which can be drawbacks.

Multi-wavelength illumination is an essential function to achieve complete control of the nerve system. However, a novel approach is needed to overcome existing constraints in light delivery and device fabrication.

1.4 Research objectives

This dissertation aims to develop a multi-wavelength light delivery probe by utilizing a newly proposed disposable MEMS optrode array for wirelessly controlled photostimulation in optogenetics. The objective comprises two closely related but separate subdivisions.

First, the modeling and fabrication of a thermally reflowed square-shaped glass microlens array.

The microlens array is a principal component of the disposable MEMS optrode array which collimates light from the LED to the optical fiber. The proposed microlens array is comprised of 16 thermally reflowed square-shaped glass microlenses inside the silicon substrate, which are fabricated via full wafer-level process.

Second, the implementation of a LED-waveguide-based light delivery probe with improved light delivery efficiency and multi-wavelength illumination.

Improving light delivery efficiency can endow the probe with the capabilities compatible for practically required light power handling and wirelessly controlled system. On the other hand, multi-wavelength illumination enables complete control over the stimulation and inhibition of the nerve system. The probe comprises a disposable MEMS optrode array and a reusable backlight unit with separable

functionality. The MEMS optrode array consists of 4×4 array of glass microlenses and 6 mm-long optical fibers in one-to-one correspondence to the fiber. The reusable unit includes a domed-top LED and a driving circuitry.

1.5 Originality and contribution

In terms of light delivery probe for photostimulation in optogenetics,

- The highest total light power, among conventional LED-waveguide-based optical neural probes, is delivered from a single commercially available LED to the distal tip of the waveguide by expanding the waveguide into an array.
- A disposable probe tip configuration is proposed to reduce the potential risks of infection from probe reuse while minimizing the wasted parts of the probe after animal experiment application.
- A multi-wavelength illumination is implemented for the first time in a LED-waveguide-based neural probe.
- A MEMS microlens array as collimating optics in a LED-waveguide-based neural probe is adopted for the first time to break through the limitation of conventional butting methods.
- A domed-top LED is utilized for the first time in a LED-waveguide-based neural probe.

In terms of the design and fabrication of the optical MEMS device,

- A simple and practical method for suppressing surface crystallization on borosilicate glass is proposed and validated for the first time.
- Modeling and fabrication of a through-substrate spherical and square-shaped glass microlens array using a thermal reflow process is proposed and validated for the first time.

2. Light delivery probe with MEMS optrode array

2.1 Introduction

Several LED-fiber-based neural probes have been presented in existing literature as possible solutions to the limitations mentioned in the previous chapter while retaining the advantages of the fiber-based configuration, by integrating segmented optical fibers and LEDs [24, 32, 33]. However, as mentioned above, these approaches employ a monolithic integration of the fibers and the light source which can cause large amounts of wasted parts and become costly as a result.

In terms of light coupling efficiency, a breakthrough is needed to move away from the conventional butting method because the method results in a considerable loss of light even in the ideal condition of maximum efficiency. Effective light delivery has become more crucial because the probes are now generally designed for wirelessly controlled systems that run on limited electricity.

As a solution to these limitations, this paper presents a light delivering probe with a separable configuration between the disposable MEMS optrode array and the reusable LED circuitry. The MOA consists of 4×4 array of square-shaped glass microlenses and high numerical aperture (*NA*) optical fibers. By developing a new structure with the MEMS technology, the proposed probe enables the dispose of the optrode while improving the light delivery efficiency. The proposed approach presents a new alternative for fiber-optic neural probe design and fabrication.

2.2 Proposal and overall design

Figure 2.1 shows the schematic diagram of the proposed light delivering probe from a cross-sectional point of view. The probe is designed to mechanically separate into two parts: the reusable LED driver unit and the disposable MOA. Both parts are assembled in separate, customized polycarbonate sheaths. A set of latch structures are included in the sheaths to enable repeated attachment and detachment. This separable configuration minimizes the waste of the parts that are inserted inside the brain during an animal experiment. Moreover, the device can be functionally improved, for example, by replacing the reusable unit with LEDs of different wavelengths, and can also enable effective response to malfunction during a long-term experiment.

The reusable unit consists of a domed-top LED and its driver circuitry. Meanwhile, the MOA consists of a 4×4 set of high *NA* optical fibers and square-shaped glass microlenses with one-to-one correspondence. The microlenses are formed on the silicon substrate and the optical path is secured perpendicular to the substrate. The substrate also has a fiber guide structure on the opposite side to support both the lateral alignment of the fibers with the microlenses and the vertical assembly to the substrate. The array in proposed probe can be effectively expanded, which is particularly advantageous for researches on large-scale neural systems or applications targeted on larger mammals such as non-human primates [7, 35] and for minimizing cell damage during insertion into the body.

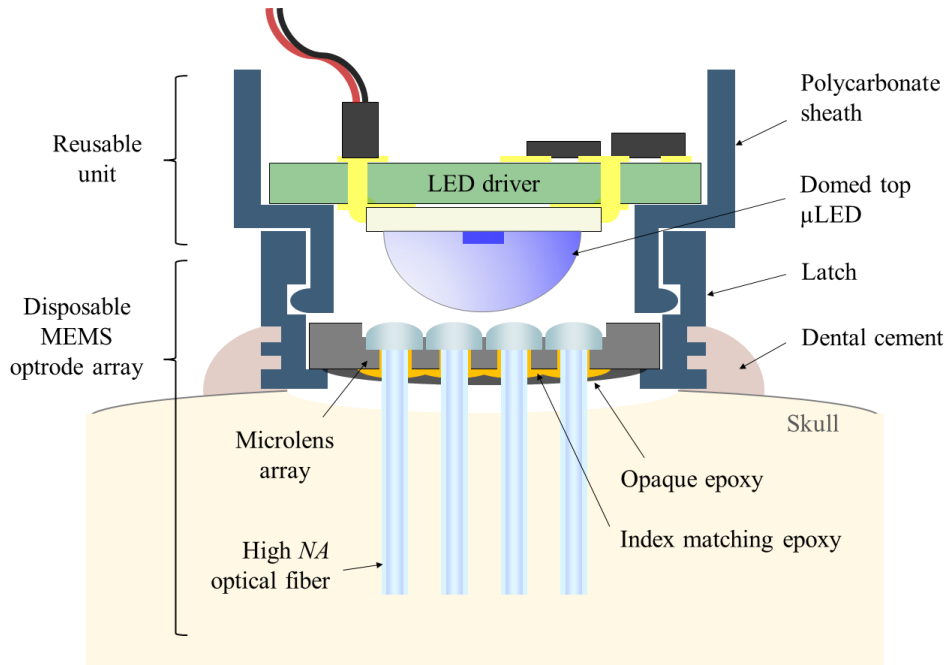


Figure 2.1. Schematic diagram of the proposed light delivering probe. The probe comprises the disposable MEMS optrode array and the reusable μ LED unit.

For proof of concept, the proposed light delivering probe was made up of 16 high NA optical fibers (FP200URT, Thorlabs) with core diameters of $200\ \mu\text{m}$ and NA of 0.5. The fibers are arranged in lattice configuration at regular intervals of $320\ \mu\text{m}$ in both direction. Contrary to a bare LED, a domed-top LED generally has a much narrower viewing angle and higher luminous intensity in the region of interest due to the integrated converging microlens. A domed-top LED (XZFBB78W, SunLED) with a p-n junction size of approximately $210 \times 210\ \mu\text{m}^2$ was selected considering the total light receiving area of the fiber array, which is $0.50\ \text{mm}^2$. Recalling [34], the calculated achievable maximum efficiency is over unity, which indicates that ideal collimating optics can theoretically achieve light delivery from the LED to the fiber

distal end with no loss. The diameter of the dome, which is assumed as the effective luminous area of the LED, and its viewing angle were $\text{Ø}1.8$ mm and $\pm 10^\circ$, respectively. Given that the selected LED has a low viewing angle, the emission of the source was assumed as a plane wave for design simplification. The microlenses were arranged to maximize the light delivery efficiency of the probe while satisfying the given geometrical and fabrication constraints. The footprint dimension of the microlenses and the gap between the microlenses were $300 \times 300 \mu\text{m}^2$ and $20 \mu\text{m}$, respectively. The surface curvature of the microlens was determined by the computational modeling described in the following section. Note that both the LED specifications and the geometrical dimension of the microlens can be modified depending on the type of optical fiber or configuration of the array required for its application.

2.3 Theoretical light delivery

2.3.1 Theoretically achievable maximum efficiency

The direct coupling of an optical fiber with a light source with Lambertian emission, namely, butting method, has to bear a considerable amount of degradation in light coupling efficiency. The maximum achievable efficiency is known to be proportional to the square of the fiber NA and the areal ratio of the fiber cross-section to the LED luminous surface, while being unaffected by additional collimating optics when the areal ratio is less than unity [34]. To improve the light coupling efficiency beyond the above-mentioned limitation, we utilized a LED whose diode has a smaller luminous area than the total light receiving area of the fiber array. The method is similar to well-known approaches for enhancing light coupling efficiency, such as coupling a bulb-ended fiber to a planar LED [36] or deploying a sphere microlens between a fiber and a domed-top LED [37]. Meanwhile, the proposed method enlarges the light receiving area rather than reducing the size of the LED to less than a single fiber cross-section by adopting a microlens array. This method can be applied using a simple manufacture procedure as it utilizes commercially available LEDs with necessary requirements.

2.3.2 Fresnel reflection

Sufficient effort was made on the detailed analysis and design to achieve efficient light power delivery. Fresnel reflection occurs at the interface between two substances of disparate refractive indices when light passes through. Figure 2.2 shows the predictable Fresnel reflections in the MEMS optrode array.

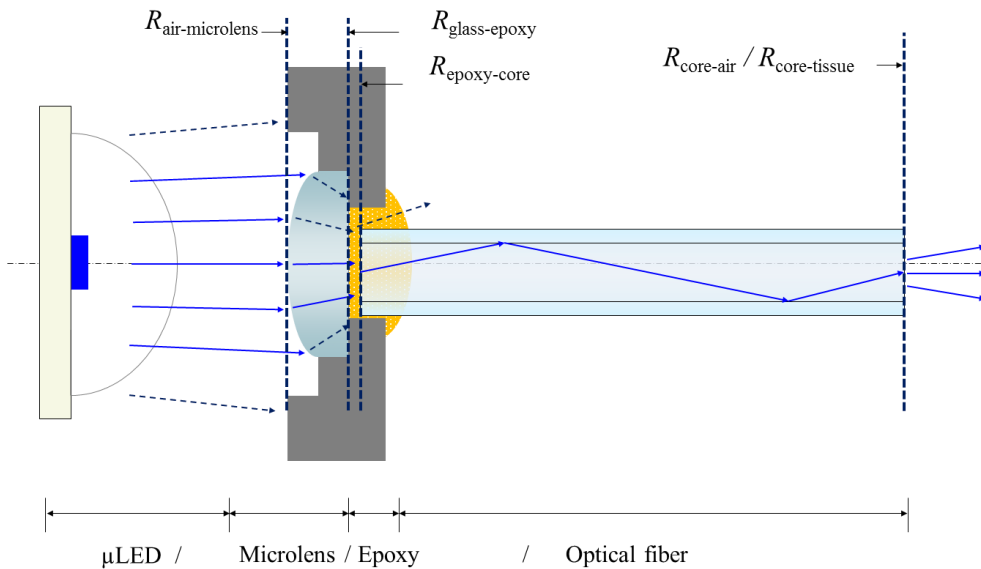


Figure 2.2. Fresnel reflections in the MEMS optrode array

When a nominal incident of light on the interface is assumed, Fresnel reflection can be simply expressed with the refractive indices of two substances as below [14]. Here, n_1 and n_2 indicate the refractive indices of the substance before and after the interface, in terms of the light propagation.

$$R = \left(\frac{n_1 - n_2}{n_1 + n_2} \right)^2$$

In Figure 2.2, the reflectance of these interfaces are notated in the form of $R_{\text{before-after}}$. It is assumed that there are four interfaces where Fresnel reflection will occur and contribute to the light loss in the system. The refractive indices considered in the analysis are summarized in Table 2.1. The refractive indices of air, BSG, and the optical fibers' core and cladding are each set to 1.000, 1.472, 1.464, and 1.376, respectively.

Table 2.1. Refractive index of substances.

Material	Refractive index	Reference
Air	1.000	[38]
Borosilicate glass	1.472	[39]
Fiber core	1.464	[40]
Fiber cladding	1.376	[40]
Index matching epoxy	1.56	[41]
Tissue	1.36	[42]

Table 2.2 summarizes the reflectance and transmittance at various interfaces in the proposed light delivering probe. In terms of animal experiment, all reflectance are negligible except the reflectance at the air/microlens interface. Nevertheless, in the device validation in the laboratory, the reflectance at the core/air interface was also taken into account.

Table 2.2. Reflectance and transmittance at various interfaces

Interface	Reflectance (R)	Transmittance (T)
Air/glass ($R_{\text{air-glass}}$)	0.036	0.964
Glass/epoxy ($R_{\text{glass-epoxy}}$)	0.001	0.999
Epoxy/core ($R_{\text{epoxy-core}}$)	0.001	0.999
Core/air ($R_{\text{core-air}}$)	0.035	0.965
Core/tissue ($R_{\text{core-tissue}}$)	0.001	0.999

2.3.3 Coupling efficiency

The proposed light delivery probe is composed of three separate optical components, which are the LED light source, the microlens array, and the optical fibers. Given that the probe is assembled with multiple components, various factors can influence its light coupling efficiency, including the numerical aperture and light transmitting or receiving area of each component, and manufactural errors and misalignments during integration that can significantly degrade the device's performance. To minimize the coupling loss within the probe, careful consideration of these matters is required.

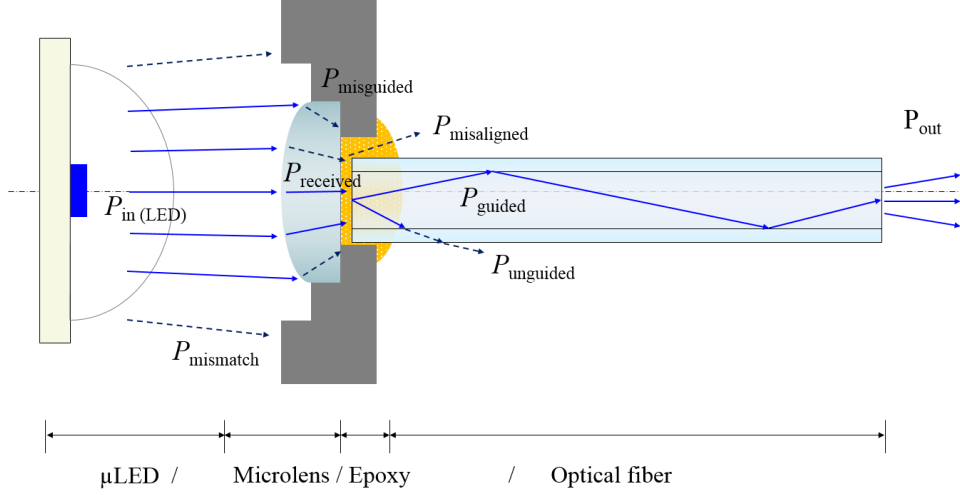


Figure 2.3. Light coupling loss in the MEMS optrode array

Figure 2.3 illustrates the light coupling loss in the MEMS optrode array including the LED. The total power transmitted from the LED will illuminate the convex side of the microlens array. However, as a necessity, there will be a light loss due to the areal mismatch between the optical apertures of the LED and the microlens array. The coupling efficiency ($\eta_{LED-lens}$) at the interface is expressed as below. To enhance $\eta_{LED-lens}$, the light receiving area of the microlens should be closely matched with the LED considering both the illumination area and the viewing angle of the LED.

$$\eta_{LED-lens} = \frac{P_{received}}{P_{in(LED)}} = \frac{(P_{in(LED)} - P_{mismatch})(1 - R_{air-glass})}{P_{in(LED)}}$$

If the viewing angle of the LED's output rays is sufficiently narrow, such as a plane wave, the above equation can be simplified as the ratio of the illumination area

of the LED and the light receiving area of the microlens array, as below. It must be noted that, here, if the areal ratio (A_{lens}/A_{LED}) exceeds unity, it is treated as unity.

$$\eta_{LED-lens} = \frac{A_{lens}}{A_{LED}} (1 - R_{air-glass})$$

After light rays are coupled to the microlens, the rays will be refracted according to the curvature of the microlens. There are three predictable losses that can occur within the microlens and the optical fiber. $P_{misguided}$ and $P_{misaligned}$ are rays blocked by the silicon aperture and the light leakage from the gap between the silicon aperture and the fiber, respectively. $P_{unguided}$ is the ray transmitted through the fiber facet which has an incident angle that is larger than the angle of total internal reflection. The coupling efficiency between the light powers coupled to the microlens and optical fiber, which is P_{guided} , can be described as below.

$$\eta_{lens-fiber} = \frac{P_{guided}}{P_{received}} = \frac{(P_{received} - P_{misguided} - P_{misaligned} - P_{unguided})}{P_{received}}$$

In sum, the following optimizations should be implemented to achieve higher total light delivery efficiency. First, the light receiving area of the microlens array should be closely matched to the illumination area of the LED light source. Second, the design and fabrication of the microlens should be carried out with sufficient consideration to minimized the light loss of $P_{misguided}$ and $P_{unguided}$. Moreover, precise alignment should be achieved during optical fiber integration on the microlens array to minimize $P_{misaligned}$.

2.4 Computational design of thermally reflowed square-shaped microlens

To improve the light delivery efficiency of the fiber-optic neural probe, this paper proposes a square-shaped glass microlens array using thermal reflow process. In the experimental environment, the MOA faces living cells on the one side and the LED on the other. In this sense, glass microlenses can be advantageous in terms of both biocompatibility and thermal stability.

Despite the inferior optical performance due to its asymmetric curvature radius and consequent light dispersion at the focal plane, a square-shaped microlens can be more efficient in terms of light delivery because of its higher fill-factor compared to a spherical microlens. A square-shaped microlens can achieve full fill-factor except for the marginal loss that occur from the fabrication constraint, that is, the silicon gap between microlenses as illustrated in Figure 2.4. In comparison, a spherical microlens has a relatively lower fill-factor of -22% and -9% in lattice and hexagonal configuration, respectively.

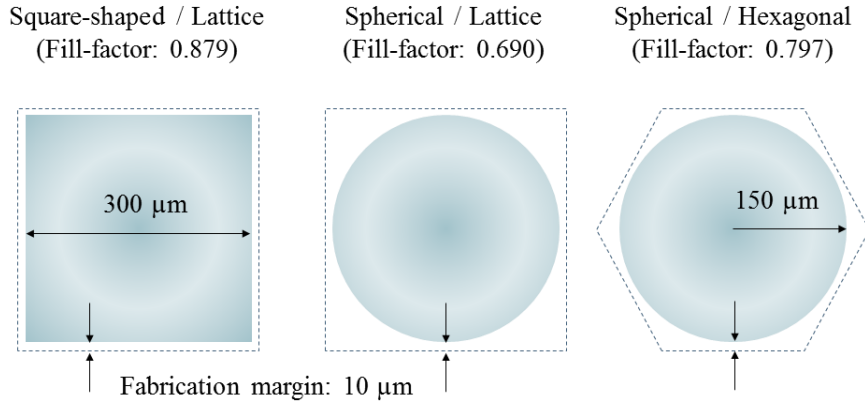


Figure 2.4. Comparison of the effective light receiving area of the microlens arranged in array

FEM simulation on computational fluid dynamics (CFD) and geometrical optics were sequentially carried out to obtain the optimized geometry of the microlens for delivering maximum light power from the LED to the fiber distal end. The modeling and microfabrication of spherical glass microlenses using a thermal reflow process have been previously validated [43]. However, despite of the well-organized reports on the numerical modeling of thermally reflowed square-shaped microlenses [44, 45], there still lacks theoretical bases for fluid dynamics.

As depicted in Figure 2.5(a-b), the square-shaped microlens for the proposed probe was fabricated by annealing a square column above its softening temperature. A two-phase level set method was utilized to find the stable geometry of the microlens as a function of the initial column height T which ranged from 15 to 55 μm. The dynamic viscosity of the molten borosilicate glass (BSG) was set to 1.82 MPa·s. The reliability of the result was validated by measuring volume constancy before and after the thermal reflow process. The effective annealing time was 40

minutes based on the evaluation of the saturation point of the maximum fluid velocity.

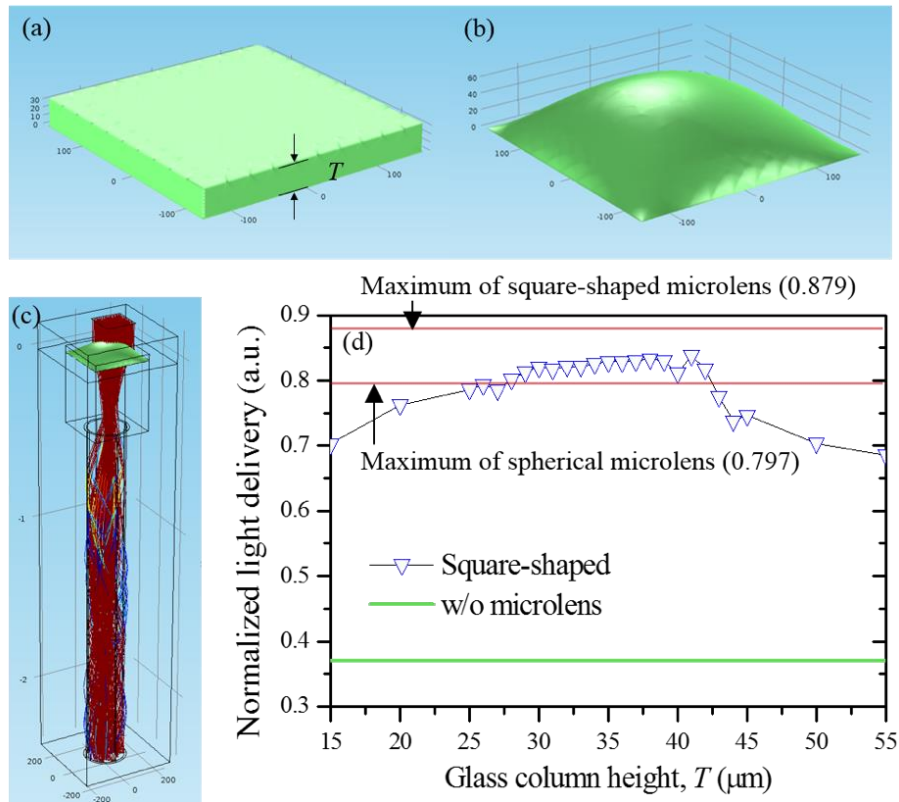


Figure 2.5. FEM simulation results of (a-b) the reflow modeling of square-shaped microlens, (c) ray tracing through the reflowed microlens, and (d) normalized light delivery as a function of glass column height prior to the thermal reflow process

The light delivery efficiency was evaluated by comparing the initial power emitted on the microlens to that at the fiber distal end using ray tracing simulation (Figure 2.5(c)). To account for the loss caused by the fill-factor, the silicon gap surrounding the microlens was included in the geometry. The light rays were assumed as 470 nm-wavelength plane waves, which have uniform intensity distribution and normal incidence. Although defining the light-emitting properties of

the LED more precisely will render more meaningful simulation results, this assumption greatly simplifies the design process. It was also assumed that the microlens and the optical fiber are in direct contact and the Fresnel reflection on the interface between reflowed microlens and ambient air was neglected.

The simulation results are summarized in Figure 2.5(d). The light delivery efficiency of the square-shaped microlens showed to be more higher than the spherical microlens in the range of 30 μm to 40 μm , since the fill-factor of the spherical microlens is 0.797, which is the achievable maximum efficiency in the given geometrical condition. From the result, T was set to 35 μm , which has the normalized light delivery of 0.83 because the efficiency at $T=35 \mu\text{m}$ is near the maximum value and less affected by the fabrication margin.

2.5 Conclusion

This present chapter described the overall design, and the numerical and computational design of the proposed neural probe.

Consequently, the total light delivery can be summarized as below equation, where P_{out} is the product of P_{guided} and the transmittance at the facet of the fiber distal end ($1-R_{fiber-air/tissue}$). Based on the equation for total light delivery efficiency, the cause of light loss and the efficiency of the proposed neural probe are summarized in Table 2.3. The total efficiency (η_{total}) of the probe is expected to be -3.04 dB.

$$\eta_{total} = \frac{P_{out}}{P_{in(LED)}} = \frac{A_{lens}}{A_{LED}} (1 - R_{air-glass}) \times \eta_{lens-fiber} (1 - R_{core-air/tissue})$$

Table 2.3. Estimated light delivery efficiency of the proposed neural probe

Cause	Efficiency
Fresnel reflection	-0.32 dB
Areal mismatch (A_{lens}/A_{LED})	-2.47 dB
MOA ($\eta_{lens-fiber}$)	-0.25 dB
Total	-3.04 dB

3. Suppression of surface crystallization on borosilicate glass

3.1 Introduction

3.1.1 Surface crystallization

Glass is one of the most widely studied material in the microfabrication industry and academia. Various forms of glass from pure silica to silicate glass have been developed and optimized to meet the market's diverse demands. General advantages of glass, e.g., its physical and chemical stability, biological compatibility, high transparency, high thermal and electrical insulation, have placed the material in a unique position in the present field of interest.

Glass is molded in the desired structures for microsystems generally using the following three methods: reactive ion etching (RIE), wet chemical etching, and thermal reflow process. However, for three-dimensional (3D) structuring, RIE and wet chemical etching present a few technical issues. Using RIE, it is hard to realize high aspect ratio 3D structures because of the slow etch rate, which, however, can be beneficial in terms of physical and chemical stability. In addition, choosing a masking material with an adequate fabrication procedure requires careful discretion to secure selectivity during the etching process. On the other hand, the use of wet

chemical etching is limited to a few specific designs because of the characteristics of isotropic etching with hydrofluoric acid solutions.

For these reasons, thermal reflow process is widely acknowledged as the most effective method in fabricating complicated 3D glass structures. Thermal reflow process utilizes the viscosity of glass during high temperature annealing and an adequate mold structure, and its applications include packaging substrates [46, 47], microprobe [48], pressure sensor [49], microlens [50] and microlens scanners [51, 52]. The most widely-used silicate glass is borosilicate glass (BSG) because of its highly compatibility to standard semiconductor fabrication.

One of the innate characteristic of BSG during high temperature annealing is crystallization. Glass crystallization refers to the nucleation of the cristobalite, a polymorph of silica, when the glass is heated above the glass transition temperature. The crystallization can be grouped into surface and bulk crystallization depending on the place it arises and its mechanism [53]. Surface crystallization significantly increases the surface roughness of the glass and precipitates micro-cracks due to the disparity in the coefficient of thermal expansion (CTE) of cristobalites from the surrounding non-crystallized amorphous BSG [54, 55]. This can possibly degrade optical transparency to a large degree. Formation of cristobalites can also affect the optical properties of the glass because their refraction index is different [56], which can lead potential issues especially when the device is designed for micro-optical applications. Moreover, the different physical and chemical characteristics of the cristobalite can cause problems when further fabrication is necessary after the thermal reflow process [55, 57]. In addition, the insufficient number of prior researches and the lack of a standardized solution have also retarded the utilization

of the thermal reflow process in microfabrication.

3.1.2 Literature review: suppression of glass crystallization

Several factors precipitate the surface crystallization of BSG. It is well known that the amount of crystallization is both proportional to the temperature and the time of the thermal treatment. Undesired contamination during the procedure prior to the thermal reflow process also encourages the crystallization. The oxide compound ion in the BSG is known to work as a nucleus of the crystallization. Jean et al. reported in [58, 59] that, the nucleation of cristobalites in BSG is mainly caused by sodium ions. They proposed alumina [58] and gallium oxide [59] as devitrification inhibitors and increased the volume content of these metallic oxides during the sintering of BSG powders. Given that the method fundamentally changes the chemical composition of the BSG in the sintering stage, the method may not be appropriate when using commercial grade BSG for its own benefits in microfabrication.

On the other hand, the more recent work by Mogulkoc et al. [55] concluded that boron ions in BSG are the main promoter of surface crystallization instead of sodium and successfully suppressed the surface crystallization against 20 hours of heat treatment at a temperature of 700 °C by depositing a 500 nm-thick silicon nitride film. However, the experimentation failed for higher annealing temperatures and/or longer time periods. It is critical to guarantee sufficiently high temperature, e.g. beyond the softening point of glass, when forming glass structures via the thermal reflow process because the temperature directly determines the viscosity of glass and

affects the design and critical dimensions of the structure [60].

3.2 Proposal and method

The present chapter examines the effect of plasma treatment using three different reactive gases, CF_4 , SF_6 , and Cl_2 , on the surface crystallization of a commercial grade BSG wafer (Borofloat[®] 33, Schott AG, Germany) during several hours of a thermal reflow process to verify the optimal procedure for suppressing the nucleation of cristobalites. Both the BSG-air and BSG-silicon interfaces are observed. The change in surface ion concentration of BSG caused by the plasma treatments were investigated using X-ray photoemission spectroscopy (XPS) to derive the factor that inhibits crystallization. Surface characterization was conducted using scanning electron microscope (SEM) images, surface roughness, and optical transparency measurement. The proposed treatment is appealing because it significantly improves the surface quality of the thermally reflowed BSG with a simple one-minute procedure. This chapter will conclude with a practical but simple guideline for a proper thermal reflow process when handling BSG.

The glass material used in the experiment was a commercial-grade 500 μm -thick BSG wafer, Borofloat[®] 33, supplied by Schott AG, Germany [39]. A typical BSG chemically consists of 81 wt% SiO_2 , 13 wt% B_2O_3 , 4 wt% $\text{Na}_2\text{O}/\text{K}_2\text{O}$, 2 wt% Al_2O_3 . The transition temperature and the softening point of the glass are 525 °C and 820 °C, respectively.

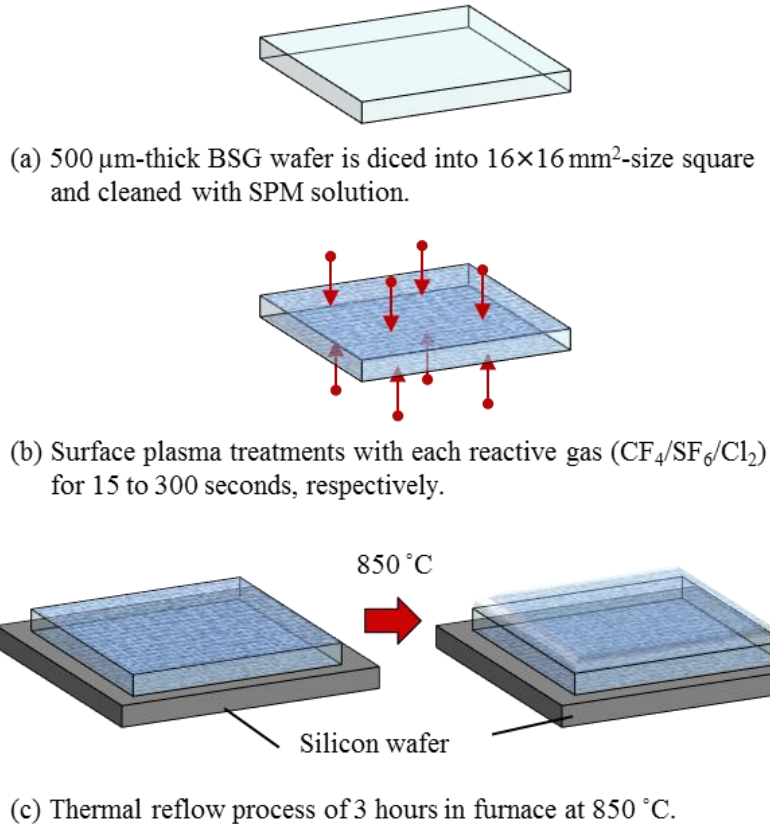


Figure 3.1. Schematic diagram of sample preparation procedure

Schematics of the sample preparation procedure is illustrated in Figure 3.1. A BSG wafer was diced into a square plate with an areal size of $16 \times 16 \text{ mm}^2$. The glass plates were cleaned using a standard SPM solution ($\text{H}_2\text{SO}_4:\text{H}_2\text{O}_2 = 4:1$). After rinsing with deionized water, the samples were dipped in IPA solution and dried in an oven at $90 \text{ }^\circ\text{C}$ (Figure 3.1(a)). The RF plasma treatments (Plasmalab 80Plus, Oxford Instruments, UK) were performed with three different reactive gases, CF_4 , SF_6 , and Cl_2 , on both sides of the glass plate to examine both BSG-air and BSG-silicon interfaces (Figure 3.1(b)). The flow rate of the reactive gases was identical to 50 sccm and the treatment time was split up in five intervals from 15 seconds to 300

seconds. The pressure inside the chamber during the process was 55 mTorr and the forward power of RF generator was 150 W. After plasma treatment, the surface ion concentration was measured with X-ray photoemission spectroscopy (XPS, Sigma Probe, VG Scientific, UK). Glass plates were placed on a silicon bare wafer to prevent melt on a quartz chuck of the mini furnace. Thermal treatment was done using a mini furnace (SMF-800, Seoul Electron Inc., Korea) (Figure 3.1(c)). The temperature was elevated up to 850 °C in 2 hours (7 °C/min) and maintained for 3 hours, then cooled down to room temperature by power off. The temperature was cooled down to 100 °C in around 3 hours (-4.2 °C/min).

The amount of crystallization was investigated by directly counting the number of cristobalites through an optical microscope (STM6, Olympus, Japan). FE-SEM (S-48000, Hitachi, Japan) was used to closely inspect the shape of the cristobalite and the surface morphology. Average surface roughness was measured using a 3D surface profiler (μ Surf, NanoFocus, Germany). The samples were separated from the silicon wafer by removing the silicon using a 20 wt% Tetramethylammonium hydroxide (TMAH) solution. Reactive ion etching was applied to remove any residual silicon remained on the glass plates. Optical transparency was measured using a UV/VIS/NIR spectrophotometer (Cary 5000, Agilent Technologies, US).

3.3 Results and discussion

3.3.1 Suppression of surface crystallization

Figure 3.2 shows the measured optical images of the glass plates after 3 hours of thermal reflow process at 850 °C. Each set of images, (a-b), (c-d), (e-f), and (g-h), indicate untreated, reactive gas of CF₄, SF₆, and Cl₂, respectively. The left (a, c, e, g) and the right images (b, d, f, g) were taken by focusing on the BSG-air and BSG-silicon interfaces, respectively. The circles in Figure 3.2 (c) to (h) were intentionally marked on the images to indicate the cristobalites on the corresponding image plane. The blurred pattern on all figures are from the cristobalites on the other side of the glass plate. The results from all three plasma treatments showed drastic suppression of the surface crystallization on both BSG-air and BSG-silicon interfaces compared to untreated sample.

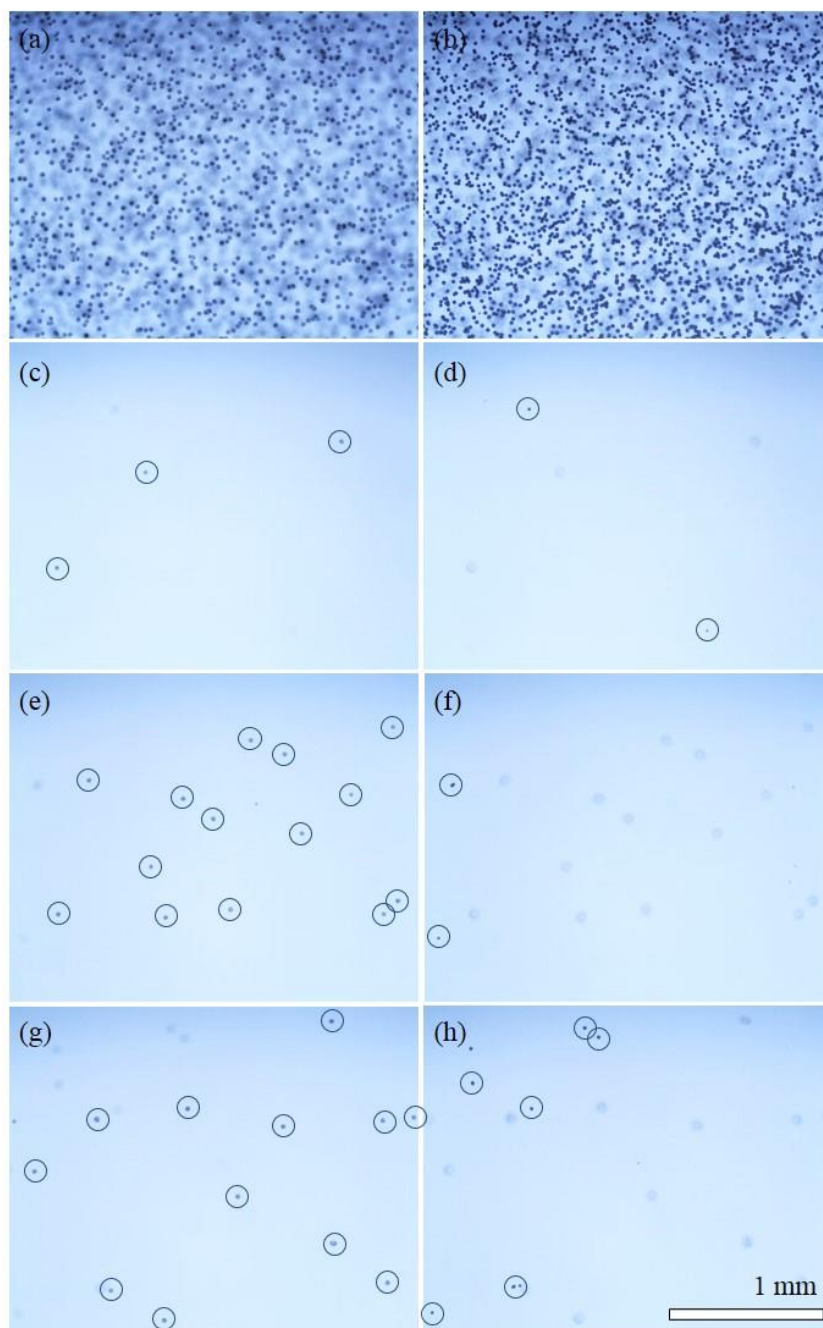


Figure 3.2. Optical images of BSG surface after the 3 hours of thermal reflow process at 850 °C. (a-b) Untreated, (c-d) CF_4 / 5 min, (e-f) SF_6 / 5 min, (g-h) Cl_2 / 5 min. The left (a, c, e, g) and the right images (b, d, f, g) were taken focusing on either BSG-air and BSG-silicon interface, respectively. Circles marked in the figures indicate the

cristobalites observed in the image plane.

The number of cristobalites on the BSG surface as a function of plasma treatment period is summarized in Figure 3.3. Plasma treatments with CF_4 and SF_6 reactive gases precipitated the drastic suppression of crystallization down to a few cristobalites per square millimeter, compared to that of the untreated sample, which was over 300 per square millimeter. After no fewer than 30 seconds of both CF_4 and SF_6 plasma treatments, the effect of the treatment on suppressing crystallization was near saturated. Then, negligible difference was found up to 5 minutes of treatment period. On the other hand, in the case of Cl_2 plasma treatment, a clear relationship between the treatment period and the amount of crystallization was observed. After 5 minutes, however, Cl_2 reactive gas also suppressed the nucleation of cristobalite down to that of SF_6 reactive gas, which was around 2 per square millimeter. As can be confirmed from these results, the proposed method can simply and effectively prevent surface crystallization during 3 hours of thermal treatment at high temperature.

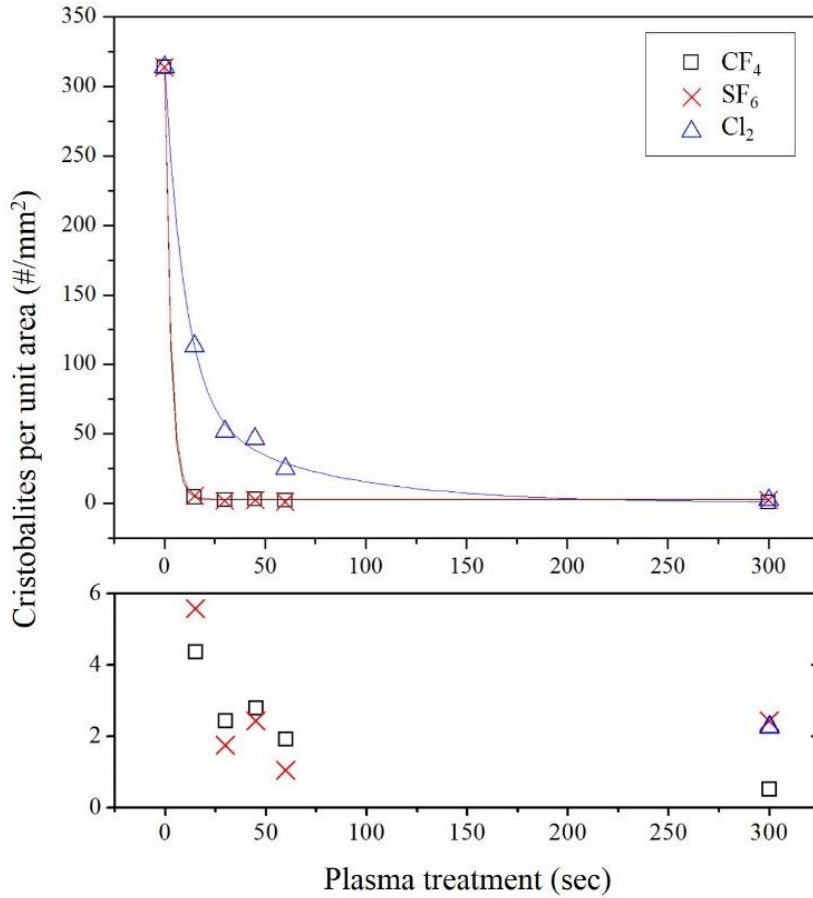


Figure 3.3. The number of formed cristobalites on BSG surface as a function of plasma treatment period. The below graph is magnified view on the results of CF_4 and SF_6 reactive gas.

3.3.2 Surface ion concentrations and roughness

Figure 3.4 shows the change in the surface concentration of ions contained in impurity oxides (boron, sodium, aluminum, potassium) as a function of the three plasma treatments, measured using XPS. The general tendency of ion concentration

mainly arises from the volatility of the fluoride and chloride compounds generated during the plasma treatments [61, 62]. Note that the boiling point of the various compounds, possibly generated during either CF_4 , SF_6 , or Cl_2 plasma treatments, are as follows: SiF_4 -86.0°C , BF_3 -101°C , NaF 1704°C , AlF_3 1276°C , KF 1502°C , SiCl_4 57.7°C , BCl_3 12.7°C , NaCl 1465°C , AlCl_3 120°C , KCl 1420°C . The surface ion concentration of volatile species such as SiO_2 and B_2O_3 relatively decreased during all three plasma treatments. Meanwhile, those of non-volatile species including Na_2O , K_2O , and Al_2O_3 increased as a function of plasma treatment time.

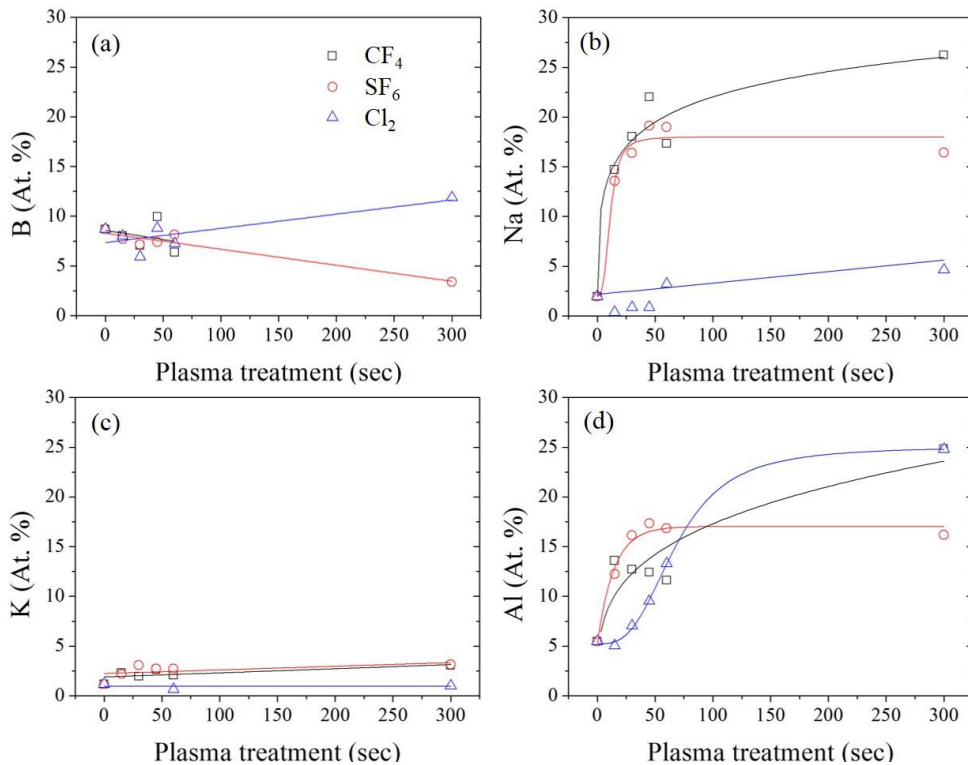


Figure 3.4. X-ray photoemission spectroscopy results. Surface ion concentration as a function of the plasma treatment time. (a) Boron, (b) sodium, (c) potassium, (d)

aluminum

Considering the amount of crystallization in Figure 3.3, crystallization showed sharp decline with fluorine plasma treatment, and relatively gradual decline when plasma-treated with chloride. However, it was not possible to explain the changes in the ion concentrations of B, Na, and K and their effects on crystallization suppression. On the other hand, the ion concentration of Al, which exists as Al_2O_3 in the BSG, was closely proportional to the suppression of crystallization. This result corroborates with existing literature [58]. Through the quantitative analysis of the crystallization and surface ion concentration, the dominant cause behind crystallization suppression was verified to be the increase of the surface ion concentration of alumina during plasma treatment.

3.3.3 Surface characterization

Surface morphology and optical transparency were investigated to verify the utility of the proposed method in micro-optical applications. A 150 nm aluminum film was deposited prior to SEM and 3D surface profile measurement to minimize the charging effect and to secure complete reflectance. Figure 3.5 shows the measured SEM image of the surface of the untreated sample after the thermal reflow process. As with the optical inspection above (Figure 3.2 (a)), high areal density of crystallization was clearly confirmed. The cristobalites showed consistent sizes within around 30 μm in diameter. The presence of cristobalites was also verified with

the presence of micro-cracks, which form due to the disparity of the CTE between cristobalites and neighboring amorphous BSG. The bright light pattern was caused by the charging effect.

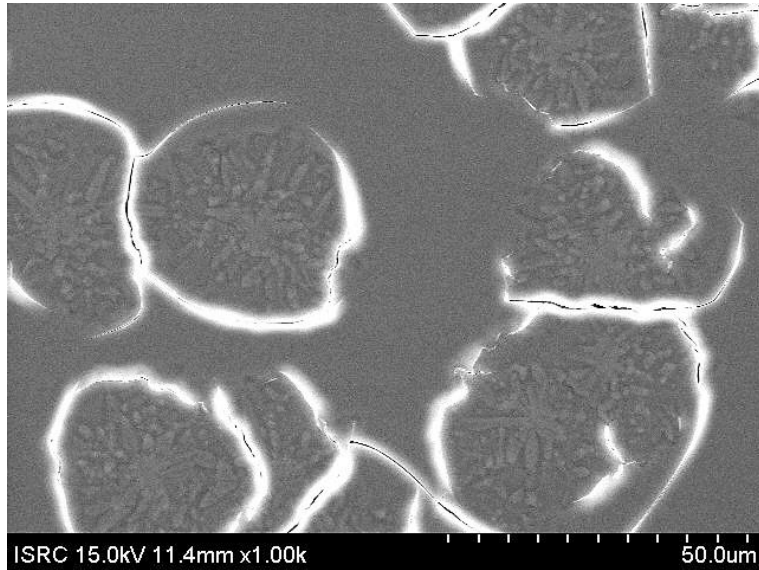


Figure 3.5. SEM image of the cristobalites and induced micro-cracks on reflowed glass surface.

Figure 3.6 summarizes the morphology of the reflowed glass surfaces. Figure 3.6 (a) is the magnified image taken from the cristobalite surface of the untreated surface. Figure 3.6 (b), (c), and (d) were taken from the uncrystallized domain of the samples after plasma treatment of CF_4 , SF_6 , and Cl_2 for 5 minutes, respectively. Analogous surfaces composed of grain sizes under 30 nm were found in all samples with no particular crystalline structures in the sub-micrometer scale. Through the close inspection of the reflowed glass surface, it was possible to assume that the amount of cristobalites formed among the samples dominantly affects surface

qualities such as surface roughness and optical transparency.

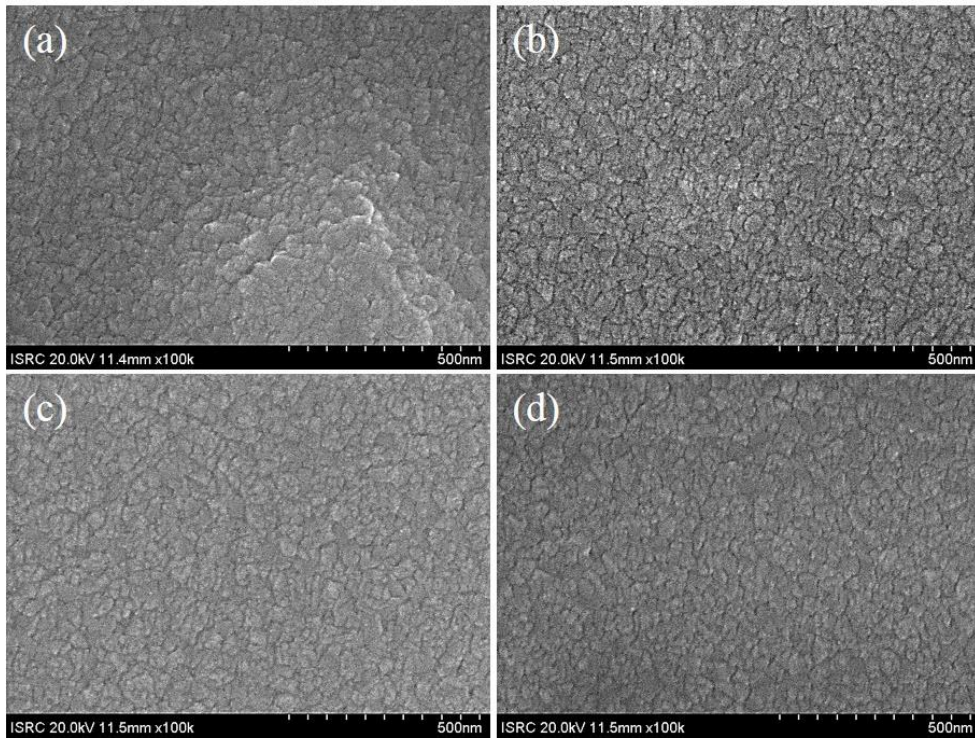


Figure 3.6. SEM images of the reflowed glass surfaces.(a) Surface of the cristobalite from untreated sample and uncrystallized surface of samples with plasma treatment; (b) CF_4 / 5 min, (c) SF_6 / 5 min, (d) Cl_2 / 5 min.

Figure 3.7 shows the measured surface profile within the area of $1.6 \times 1.6 \text{ mm}^2$ at the center part of the samples. All samples applied with surface plasma treatments were verified to have appropriate average surface roughnesses in the order of tens-of-nanometer. The proposed method was highly effective considering that the average surface roughness of the plasma treated samples were enhanced 15 times than the untreated sample, which was 672 nm.

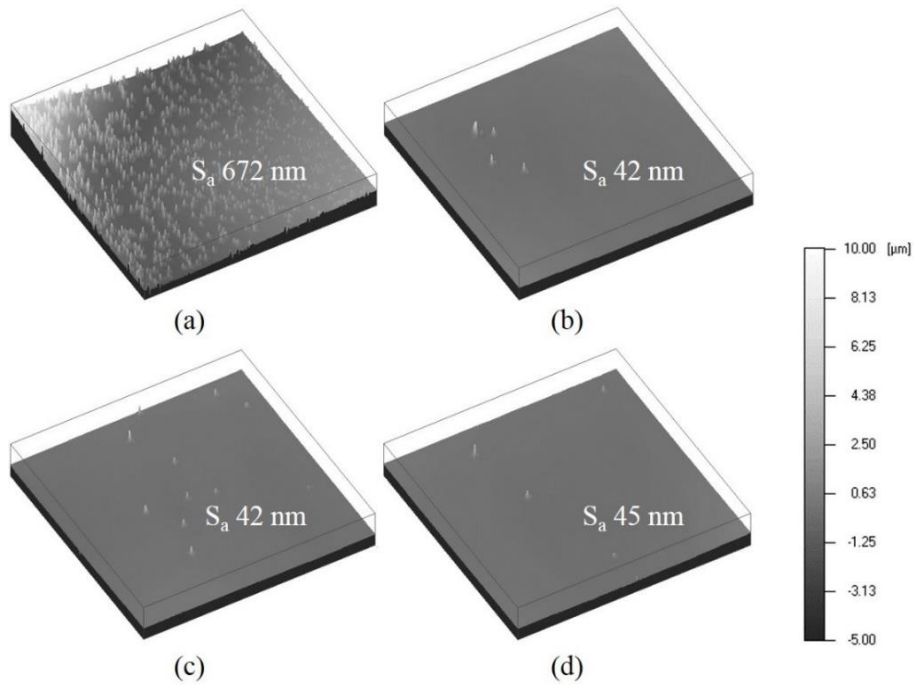


Figure 3.7. Measured surface profile within area of 1.6x1.6 mm² at the center part of the glass samples using confocal-based 3D surface profiler. (a) Untreated, (b) CF₄ / 5 min, (c) SF₆ / 5 min, (d) Cl₂ / 5 min.

Optical transparency measurement results are shown in Figure 3.8. From 200 nm to 1500 nm range of wavelength, the average transparency was measured to be slightly low compared to the known transparency of the 500 μm-thick Borofloat[®] wafer. The result was, however, valid for vitrification, given that the samples with suppressed crystallization had 3 times better transparency compared to that of the untreated sample. The general degradation of transparency among the samples was possibly due to post procedures such as TMAH wet chemical etching and reactive ion etching for separating the samples from the silicon wafer.

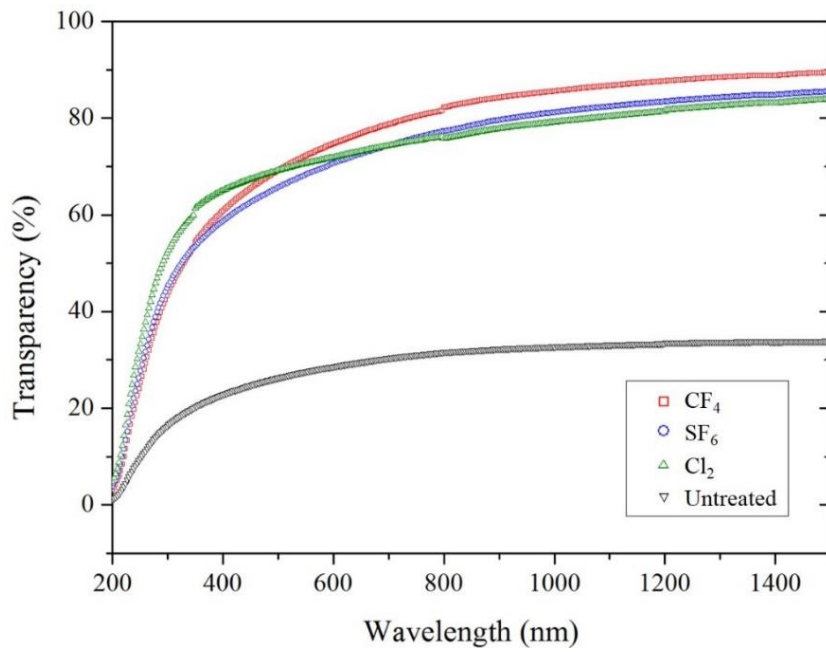


Figure 3.8. Optical transparency measurement.

3.4 Conclusion

Surface crystallization on commercial grade borosilicate glass, Borofloat[®] 33, was effectively prevented during 3 hours of heat-treatment at 850°C. Quantitative analysis of the crystallization and surface ion concentration verified fluorine plasma treatments of no fewer than 30 seconds to be significantly effective in suppressing the nucleation of cristobalites. The average surface roughness and optical transparency were enhanced 15 and 3 times, respectively, compared to the untreated sample. The results highly suggest the suitability of this simple and practical method for vitrification in BSG during a thermal reflow process.

4. Through-substrate square-shaped glass microlens array

4.1 Introduction

4.1.1 MEMS microlens and microlens array

In recent years, micro-optics has gained an increasing amount of attention from both the industry and the academia. The micro-opto-electro-mechanical system (MOEMS) has been a principal force in the miniaturization of optical devices from bulk optics, with a growing number of applications in various fields such as optical communications, imaging, optoelectronics and photonic devices.

As with micromirrors [63-65], MEMS microlenses are commonly used in optical systems as a core component. Examples include optical scanners for lateral or depth scans [66-70], wavefront analyzers [71], and optical cross connects [72]. In the abovementioned devices, the fabrication and assembly of microlenses can significantly affect the achievable functionalities and the degree of integration in the system.

Several studies have introduced methods of fabricating and integrating microlenses with peripheral structures. One typical method utilizes a conventional SOI (silicon-on-insulator) process on commercially available microlenses [68-70]

when fabricating the electrostatically driven lateral stage. In this stage, the microlenses are manually assembled using an ultraviolet curable adhesive or an additional shuttle device. Another typical method involves curing liquid polymer droplets. Polymers such as polydimethylsiloxane or photoresist are directly pipetted onto a movable stage and formed into a semi-spherical microlenses with the assistance of surface tension [66, 67, 71, 72].

In both methods, however, it is difficult to avoid the complicated manual process involved in either fabricating the microlenses or assembling the microlenses and peripherals to often result in non-batch fabrication, low yield, and high cost. Moreover, the assembled microlenses are often not compatible with further semiconductor fabrication processes such as photolithography, dry etching and wet etching.

Glass is be a practical candidate material to solve the above issues, as it is naturally strong against circumstances such as high temperatures, high vacuums, and plasma etching, which are all commonly used in the semiconductor fabrication process. Glass is also suitable as a material for microlenses due to its excellent optical characteristics in the visible wavelength.

Manufacturing 3D glass structures can be suitably achieved using the thermal reflow process, as opposed to either dry etching or wet etching. Various strategies have been demonstrated for attaining wafer-level fabrication of glass microlenses utilizing thermal reflow with the help of either negative pressure [73], cross-cut dicing [74], wet-etching [75], laser direct writing [76], or compressive molding [50, 77]. Furthermore, as with a cured polymer droplet, low surface roughness is generally easy to achieve for thermally reflowed glass microlenses by virtue of the

surface tension. However, controlling the surface profile while successfully assembling the glass microlenses on the structural layer with precise alignment remains as an issue to be addressed.

4.1.2 Monolithically integrated glass microlens

An illustration of a monolithically integrated glass microlens substrate is as shown in Figure 4.1. In previous work, 1D and 2D microlens scanners are developed by simply patterning a comb-drive actuator around a microlens embedded in the glass microlens substrate [43, 52]. We adopted the conventional thermal reflow process which is used for fabricating polymer microlens arrays [78]. However, instead of photoresist islands on the substrate, through-silicon glass cylinders were created and transformed into microlenses via the thermal reflow process. The microlenses were fabricated in a full wafer-level process while simultaneously assembled within the silicon layer with precise alignment.

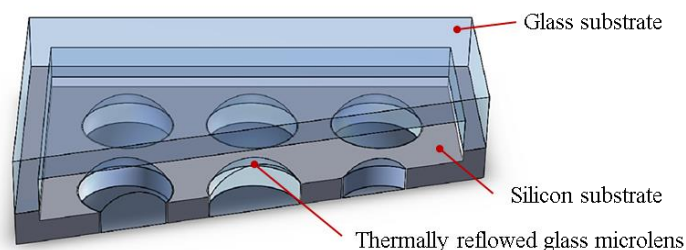


Figure 4.1. Monolithically integrated glass microlens

The fabrication process of the pre-assembled glass microlens is described in

Figure 4.2. First, a 100 mm-diameter silicon wafer was cleaned with a piranha solution. A 1 μm thick SiO_2 layer was deposited on the wafer and patterned using photolithography with a 3 μm thick photoresist layer. A silicon cavity was etched using a deep reactive ion etching (DRIE) process, which defines the geometry of the glass cylinder. (Figure 4.2(a)). A borosilicate glass wafer (Borofloat[®] 33, Schott) was anodically bonded with the silicon wafer, ensuring negative pressure in the cavity (Figure 4.2(b)). A sufficiently low pressure inside the cavity is crucial, as this functions as the major force pulling down the viscous glass into the silicon cavity.

Two thermal reflow processes were applied overall during the fabrication of the microlens. After the anodic bonding, the first thermal reflow was performed in a furnace at a temperature of 850 °C for 5 hours, filling the cavity with reflowed glass (Figure 4.2(c)). The wafer was chemically-mechanically polished (CMP) to level any unevenly reflowed glass and to expose the silicon layer. The silicon was etched by means of DRIE to define the desired height of the glass cylinder (Figure 4.2(d)). The second thermal reflow served to transform the glass cylinder into a spherical microlens (Figure 4.2(e)). The temperature of the process was maintained at 850 °C, which is above the softening point of the Borofloat[®] 33, (820 °C), to ensure sufficiently low viscosity. However, the process time was shortened to 30 minutes to minimize surface devitrification [55].

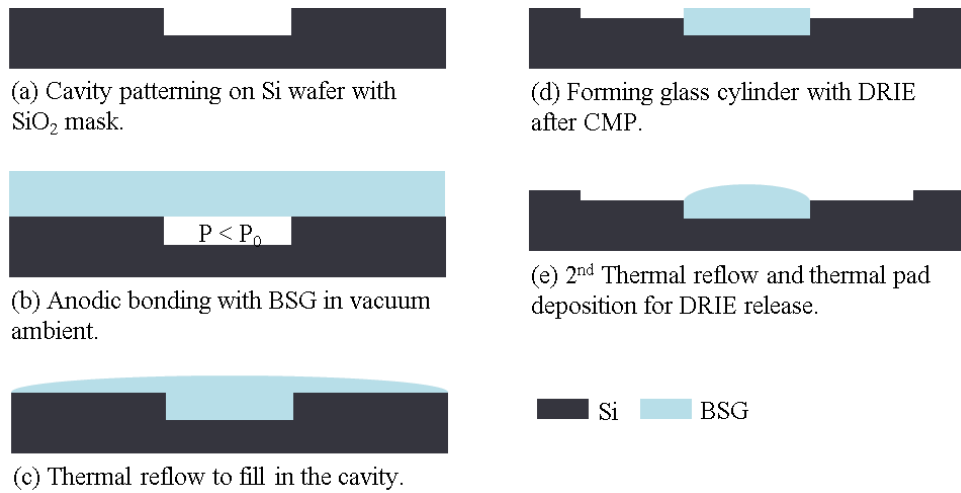


Figure 4.2. Fabrication process of the pre-assembled microlens

In general, the optical characteristics and the quality of the microlenses are two of the most important factors that determine the performance of the microlens-applied MOEMS. The nature of the microlens fabrication process and its thermal reflow steps make it comparatively easy to design and predict the surface profile of the microlens.

Because the proposed microlens was fabricated using the thermal reflow process, numerical modeling was carried out based on the following two assumptions. First, before and after the annealing, the volumes of the glass cylinder and the microlens are assumed to be constant. Second, viscous glass is assumed to have infinite surface tension, meaning that other physical factors such as gravity and the surface characteristics of the substrate were considered negligible. A schematic diagram of the microlens before and after the thermal reflow process is depicted in Figure 4.3.

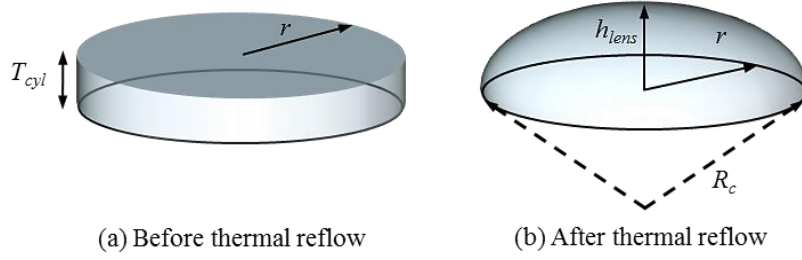


Figure 4.3. Schematic diagram of the spherical microlens before and after the thermal reflow process

Equation (4.1) is derived from the volume consistency of the cylinder and the microlens. Because the proposed microlens is assumed to exist in the form of an ideal semi-sphere, the radius of curvature (R_c) can be represented in terms of the radius (r) and the height (h_{lens}) of the microlens, as in equation (4.2).

$$\pi r^2 T_{cyl} = \frac{1}{3} \pi h_{lens}^2 (3R_c - h_{lens}) \quad (4.1)$$

$$R_c = \frac{r^2 + h_{lens}^2}{2h_{lens}} \quad (4.2)$$

Consequently, by manipulating (4.1) and (4.2), h_{lens} and R_c of the microlens can be accurately predicted from the radius r and the thickness (T_{cyl}) of the glass cylinder, as depicted in (4.3). The diameter and thickness of the glass cylinder presented in this work were 800 μm , and 64 μm , respectively.

$$h_{lens} = D - \frac{r^2}{D} \quad (4.3)$$

$$D = \frac{\sqrt[3]{162r^2T_{cyl} + \sqrt{2916r^6 + 26244r^4T_{cyl}^2}}}{3\sqrt[3]{2}}$$

Figure 4.4 shows the SEM images of the fabricated glass cylinder and the microlens before and after the second thermal reflow. The glass microlens was successfully fabricated in spherical form with a clean surface and without any defects. The surface profile of the microlens was also inspected with confocal microscopy using a 3D surface profiler (Nanofocus, μ surf). The measured value was highly consistent with the calculated profile derived from the measured dimensions of the fabricated cylinder as shown in Figure 4.5. The measured average roughness (R_a) of the microlens surface was 15 nm. Given that this value is less than 1/20 of the typical wavelength range of visible light, the device was verified as applicable in optical sensing and imaging applications.

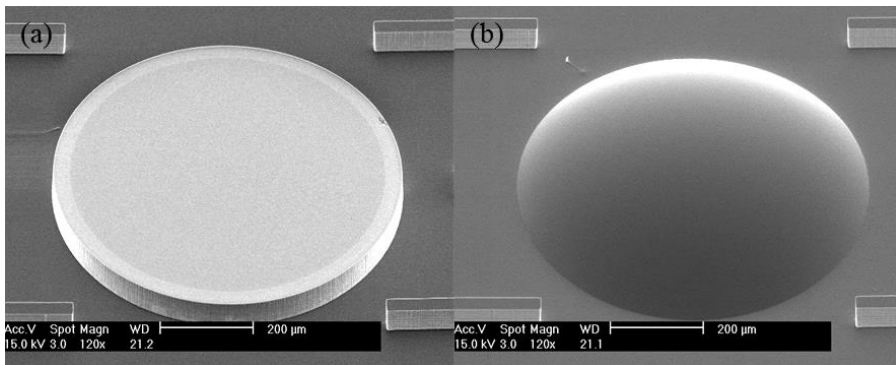


Figure 4.4. SEM images of the fabricated glass cylinder (a) and the reflowed

microlens (b)

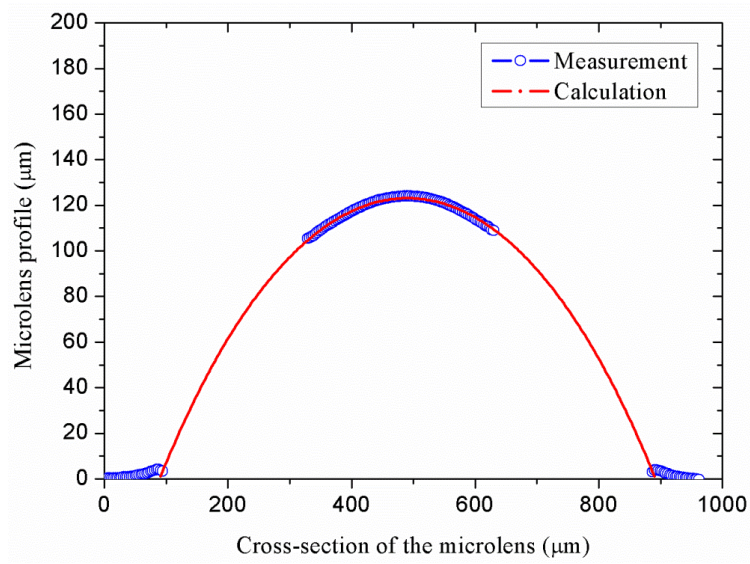


Figure 4.5. Surface profile comparison of the calculated and measured profile of the spherical microlens

4.2 Microfabrication procedure

Based on the successful validation of the thermally reflowed spherical glass microlens fabrication process above, we designed the microfabrication procedure for the square-shaped glass microlens array. The full procedure is illustrated in Figure 4.6. The first step involved cavity patterning on a 4 inch-diameter and 1 mm-thickness silicon wafer using an oxide mask and DRIE (Figure 4.6(b)). The cavity was then filled with molten BSG (Borofloat[®] 33, Schott) via anodic bonding and subsequently annealed at 850 °C for 8 hours (Figure 4.6(c)).

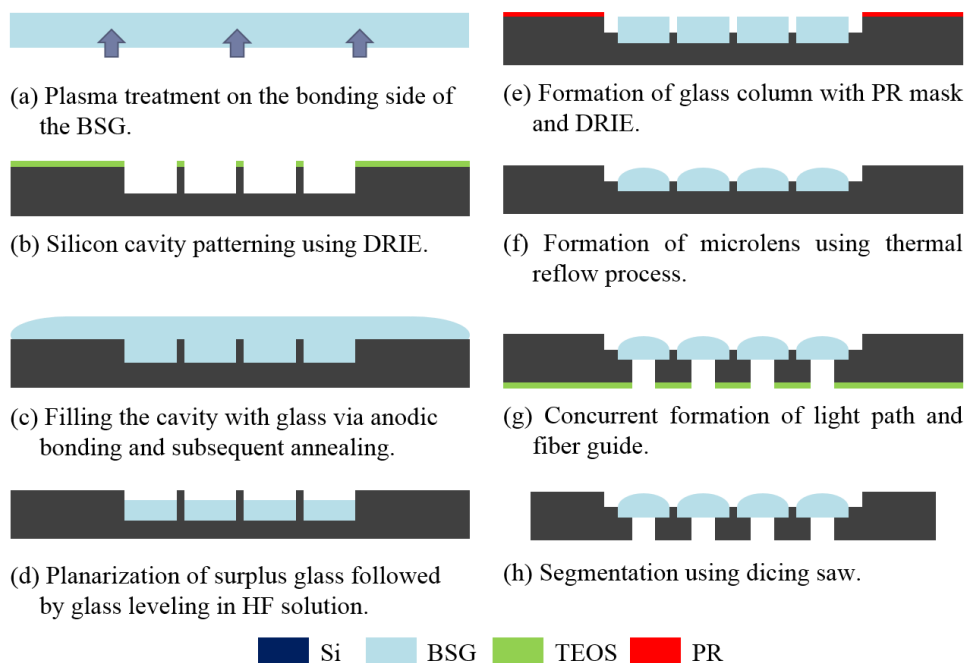


Figure 4.6. Microfabrication procedure of the square-shaped glass microlens array with fiber guiding structure

After the first thermal reflow process, the surplus glass was removed by chemical mechanical polishing, followed by a leveling down of the glass with a hydrofluoric acid solution (Figure 4.6(d)).

Plasma treatment was carried out on the surface of the BSG wafer prior to the bonding (Figure 4.6(a)) to suppress surface crystallization on the surface between the BSG and silicon [79]. Preventing surface crystallization on both the BSG/air and BSG/silicon interfaces is critical in this procedure. Crystallized BSG, the cristobalites, have different physical and chemical characteristics including a different coefficient of thermal expansion (CTE) from amorphous BSG. Thus, the cristobalites on the BSG/silicon interface can cause irregular glass geometry after the leveling process in Figure 4.6(d), which can directly affect the property of the microlenses. Moreover, the disparity in CTE can cause micro-cracks on the microlens surface during the microlens formation in (Figure 4.6(f)) and significantly degrade the optical transmittance of the microlens.

As depicted in Figure 4.6(e), BSG columns were formed using a photoresist mask and DRIE. The second thermal reflow process was carried out at the same temperature as the first reflow process and was maintained for 40 minutes (Figure 4.6(f)). Concurrent formation of the optical path and fiber guide structure was proceeded using backside DRIE. The diameter and depth of the silicon guide were 250 μm and 500 μm , respectively (Figure 4.6(g)). Finally, the microlens array was diced into 5 \times 5 mm² pieces (Figure 4.6(h)).

4.3 Results and discussion

4.3.1 Fabrication results

The fabricated 4×4 glass microlens array is shown in Figure 4.7. The scanning electron microscope (SEM) image of the microlens array verified the successful fabrication of the microlens array. However, unintended pillar-like microstructures formed in the silicon lattice area, which are speculated to be silicon near to the glass column which were not sufficiently etched during the DRIE (Figure 4.6(e)). Figure 4.7(b) shows the microscopic image at the focal plane of the microlens array when backlight is illuminated on the convex side of the microlens. The result is consistent with the SEM measurement, validating the uniform optical characteristic among the microlenses.

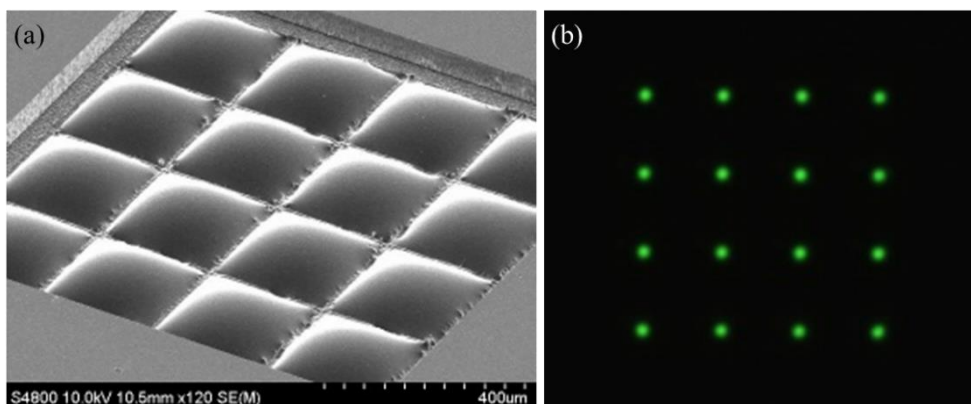


Figure 4.7. Fabrication result of square-shaped glass microlens array including (a) SEM image of the microlens array, (b) microscopic image at the focal plane when

light illuminated on the microlens

Figure 4.8 shows the microscopic images of reflowed glass surface before and after leveling in HF solution (Figure 4.6(d)). All images were focused on the glass surface. Figure 4.8(a) is the outcome without plasma treatment on glass surface prior to the anodic bonding with silicon wafer, and Figure 4.8(b), the outcome with plasma treatment. As can be seen in the Figure 4.8(a), the cristobalites that formed during the first reflow process was the direct cause of the irregular glass etching in the HF solution. The proposed surface plasma treatment clearly removed these cristobalites, as shown in Figure 4.8(b).

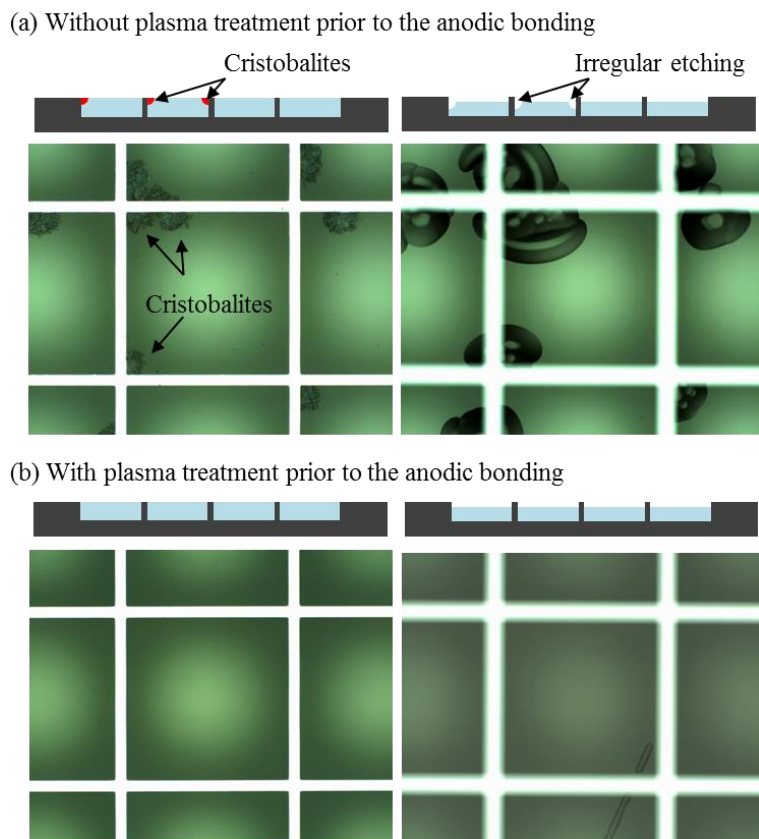


Figure 4.8. Comparison of glass leveling results between with and without plasma treatment prior to the anodic bonding

4.3.2 Surface profile and roughness

The surface profile was measured with a 3D surface profiler (Nanofocus, μ surf). The measured surface profile of the convex side of the square-shaped glass microlens array in center cross-sectional and diagonal cross-sectional views are shown in Figure 4.9(a) and Figure 4.9(b), respectively. In both figures, the black line indicates the simulation result while the blue hollow dots indicate the measured values.

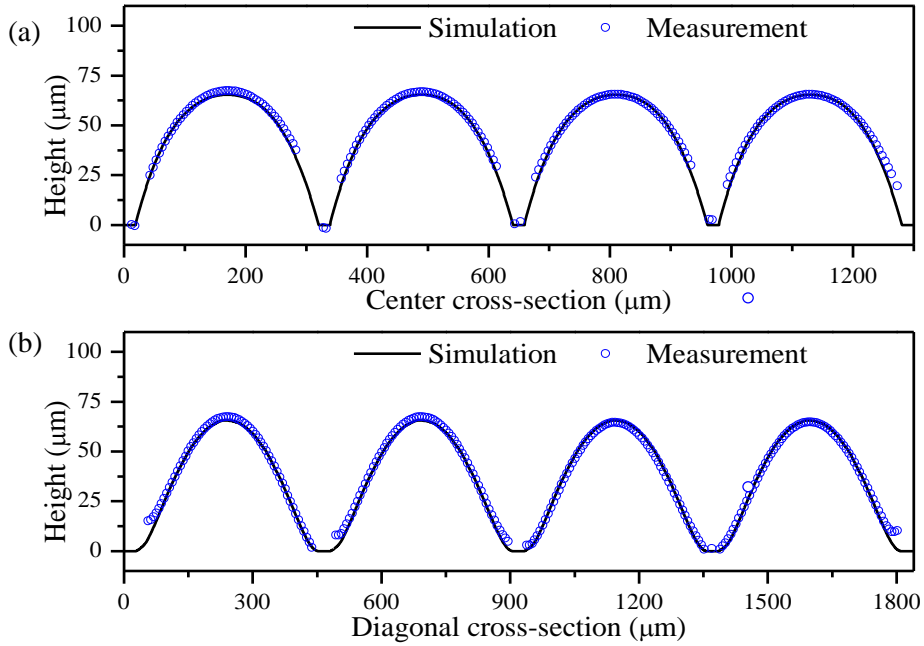


Figure 4.9. Surface profile measurement of the square-shaped glass microlens in (c) center cross-sectional, and (d) diagonal cross-sectional view

The surface profiles are in good agreement with the simulation result. The measured average surface roughness was 47 nm. Abrupt edges shown in the measured profile, also perceptible in the SEM image, in the diagonal cross-section were due to silicon pillars which occurred during the glass column formation (Fig. 4(d)) as a result of insufficient etching of silicon on the side of the column. This can be possibly removed by using an alternative mask material for DRIE such as silicon oxide or silicon nitride, which generates less silicon grass. Nevertheless, the results provide sufficient validation on the computational modeling and microfabrication of the thermally reflowed square-shaped glass microlens array.

4.3.3 Influence of oxygen plasma on crystallization

This section describes, for more robust explanation of experiment results, the influence of oxygen plasma on the surface crystallization of thermally reflowed BSG. Oxygen plasma is widely used as an effective method to remove organic polymers or metals. However, it was experimentally found that oxygen plasma before thermal annealing is strongly associated with surface crystallization during the thermal annealing.

To verify the influence of the oxygen plasma, a unit experiment was carried out. Diced glass samples were prepared in three groups. The first group was a control group while the other two groups were prepared with a 3-minute surface plasma treatment, one of SF₆ and the other of Cl₂. Then, oxygen plasma treatment was carried out on each of the three groups by standard photoresist removal procedure. Finally, all groups are thermally reflowed with the same conditions as the microlens fabrication.

Figure 4.10 summarizes the result of the unit experiment. The result clearly implies that the groups with oxygen plasma treatment prior to the thermal reflow process have much higher tendency to yield surface crystallization.

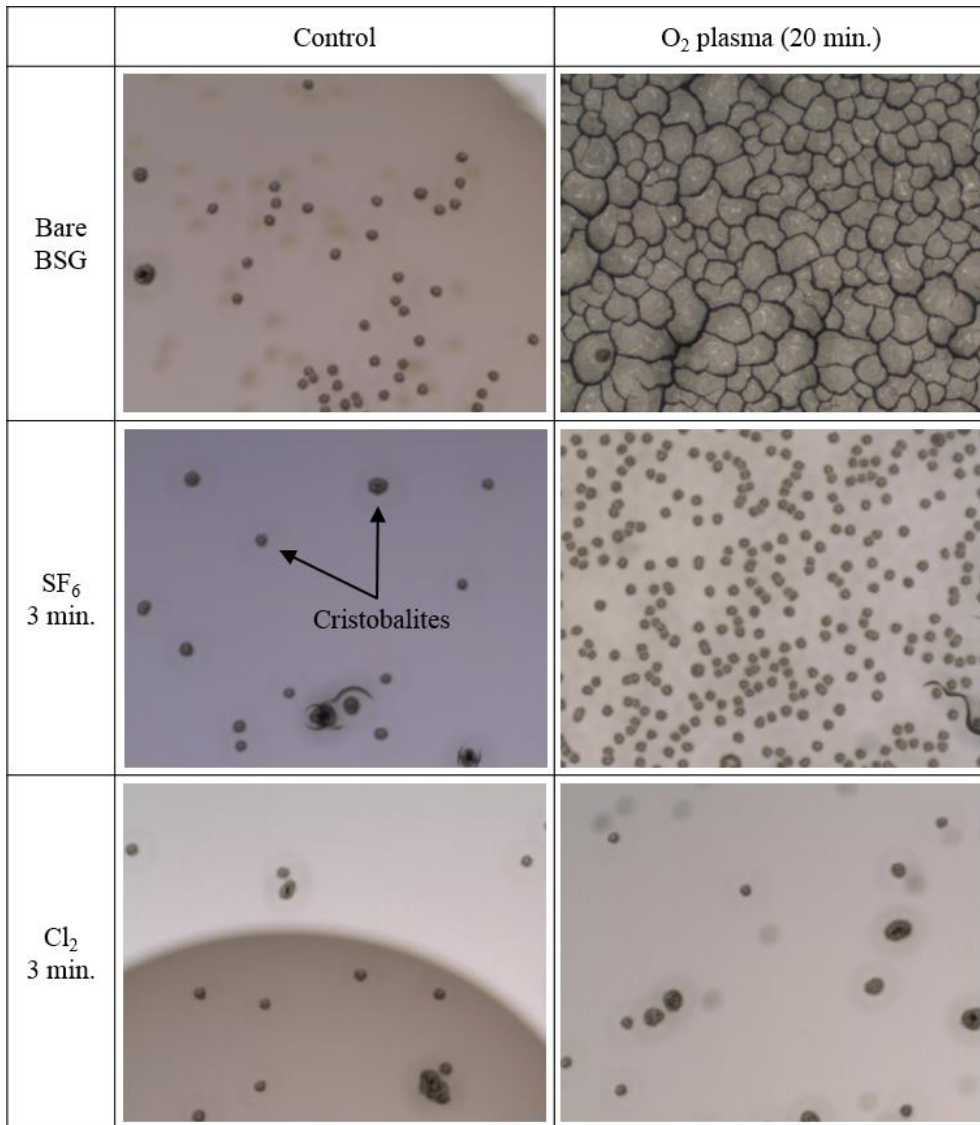


Figure 4.10. Influence of oxygen plasma on surface crystallization of borosilicate glass

4.4 Conclusion

A square-shaped glass microlens array was successfully fabricated with good agreement with the design specification. The measurement results fully validated the proposed fabrication procedure and the capability of the microlens array as a light collimating optical device in the proposed neural probe.

The present work provides validation on the design, fabrication, and characterization of both thermally reflowed spherical and square-shaped glass microlenses. However, the microfabrication procedure involves sufficient consideration of extreme high temperature process and microfluidic dynamics. As the effects of the plasma treatments with SF₆, Cl₂, CF₄, and O₂ show, there is still much to be examined in this line of research.

5. MEMS optrode array: fabrication and characterization

5.1 Introduction

In the previous chapters, a glass microlens array with optical fiber guide structure was proposed, fabricated, and characterized. Despite the clear validation of the uniform wafer-level fabrication of the glass microlens array, the proposed MEMS optrode array still involves laborious procedures after the fabrication of the microlens array such as fiber manipulation and the assembly process. As each procedure has manufactural and handling tolerance, which can possibly affect the optical performance of the probe, it is indeed important to predict potential light loss factors and reduce their causes.

This chapter describes the fabrication procedure of the MEMS optrode array including fiber segmentation and assembly. Several customized aid apparatuses are utilized to improve the accuracy of the fiber manipulation. The light delivery efficiency of the MEMS optrode array is measured, followed by analysis on the loss causes. The capability and limitations of the neural probe is evaluated in terms of the multi-wavelength illumination and disposable configuration.

5.2 Fiber manipulation and assembly

5.2.1 Optical fiber preparation

The fundamental aim of the fiber segmentation and assembly procedure is to provide optical waveguides, which are integrated on the microlens array, for safe and efficient light delivery to the target nerve system. As a commercially available 0.50 NA hard polymer clad multimode fiber (FP200URT, Thorlabs, Inc.) were utilized as the waveguide in this research, it was necessary to customize the optical fiber to meet the necessary requirements of the probe. In optical fiber preparation, optical fibers should be in uniform length and cut at an angle perpendicular to the longitudinal direction with a smooth surface.

Figure 5.1 shows the optical image of the silicon v-groove substrate, which was fabricated prior to the fiber segmentation. The fabrication of the substrate was performed, starting with a double-side-polished 4 inch-diameter silicon wafer with SPM cleaning. Tetraethyl orthosilicate (TEOS) was deposited on both sides of the silicon wafer and patterned using a standard photolithographic procedure. Then, the v-grooves were formed using a 40 wt% potassium hydroxide etchant.

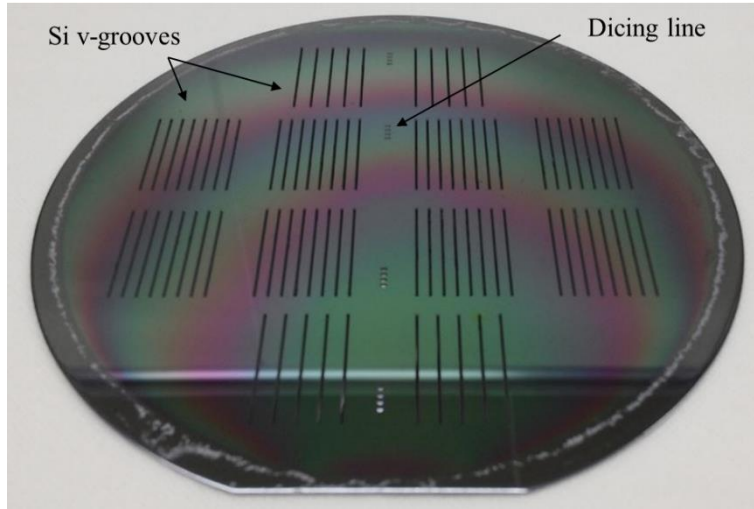


Figure 5.1. Optical image of silicon v-groove substrate for fiber segmentation.

Optical fibers were prepared through several procedures before the assembly. First, the Tefzel coating of the fiber was removed using a general-purpose fiber stripper (T12S21, Thorlabs). The optical fibers were cut with scissors into 16 mm-long segments, then placed in the silicon v-grooves and fixed with either a Kapton[®] tape or general dicing tape. The fiber segments were half-diced into the desired length, which was 6 mm for this study, to reuse the v-groove substrate. Lastly, the segmented fibers were cleaned with the aid of ultrasonic cleaner in a isopropyl alcohol solution. This procedure ensures the uniform length of the fibers and perpendicular cross-section on each side.

Figure 5.2 shows the microscopic images of the segmented optical fiber fabricated with the silicon v-grooves through the standard dicing procedure. Figure 5.2(a) shows insufficient removal of the fiber cladding, while Figure 5.2(b) shows sufficient removal. The fabrication yield was around 40%, which is relatively low.

Nevertheless, it was deemed unnecessary to improve the yield since a single dicing procedure fabricates 168 samples of fiber segment simultaneously, and superior samples were used in the assembly.

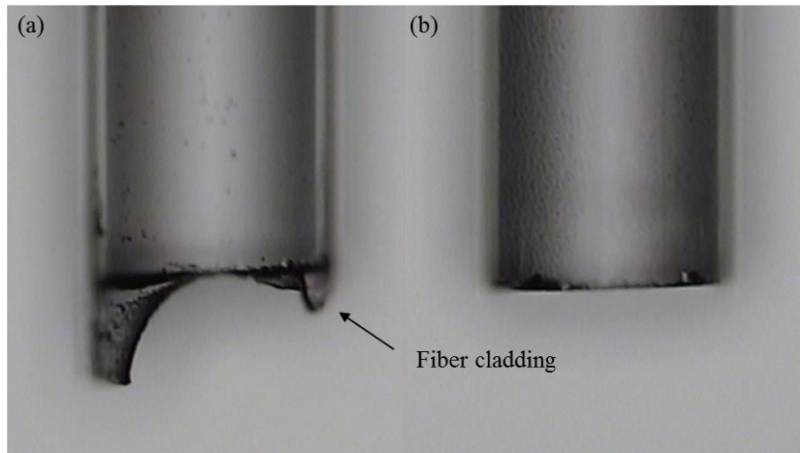


Figure 5.2. Microscopic images of facets of the segmented optical fiber using silicon v-grooves and dicing saw. (a) shows insufficient removal of the cladding, while (b) shows the sufficient removal

5.2.2 Fiber assembly

Prior to assembling the optical fibers and microlens array, an additional through-Si jig assembly guide and a custom-made aligner were fabricated. The through-Si jig was fabricated by making through-holes inside a silicon wafer with the same mask that was used in creating the optical path in the microlens array (Figure 4.6(f)). The substrate was diced into $5 \times 5 \text{ mm}^2$ pieces, same as the microlens array.

The aligner was manufactured with aluminum using micromachining. The

aligner holds the fabricated through-Si jig and the microlens array at a fixed distance in parallel to each other. This apparatus ensures that the optical fibers are perpendicularly assembled into the microlens array.

Figure 5.3 shows the microscopic image of the through-Si jig and the optical image of the micromachined aluminum aligner.

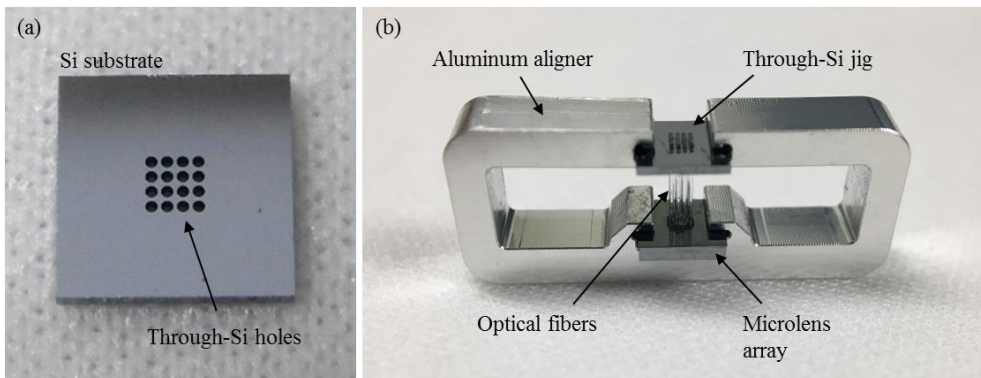


Figure 5.3. Microscopic image of the through-Si jig (a) and optical image of the micromachined aluminum aligner (b).

The optical fibers were integrated within the silicon guide structure with index matching epoxy and cured in the oven. If the cross section of the optical fiber is cut obliquely, the light coupling efficiency between the microlens and the optical fiber can be further increased. Nevertheless, dicing was used to simplify the manufacturing process by minimizing manual work during the device fabrication process and to develop a method for manufacturing uniform devices. The optical image of the fabricated MOA is shown as Figure 5.4. Optical fibers of consistent lengths were successfully assembled with the microlens array. However, either more precise dicing of the optical fiber or an additional polishing procedure should be

carried out to remove undesired residual cladding near the facet of the optical fiber.

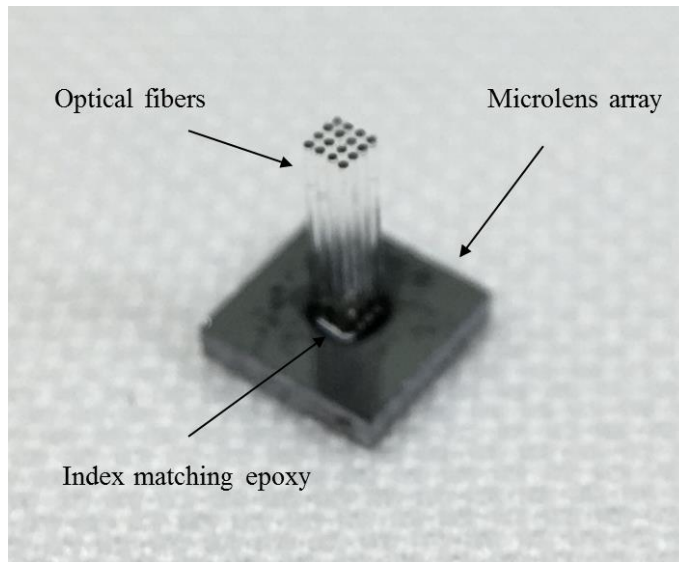


Figure 5.4. Optical image of the fabricated MEMS optrode array.

5.3 Optical characterization

5.3.1 Measurement setup

Light delivery efficiency is estimated by comparing the measured light output power between the LED and the distal end of the fiber array. The power was measured with a photodiode power sensor (S121C, Thorlabs). To evaluate the efficiency of the probe while minimizing the loss caused by inaccurate alignment, the three parts (the disposable MOA, the reusable unit, and the power sensor) were each arranged on 6-DOF stages controlled by micromanipulators. Then, repeated manipulation was carried out until the light output power was maximized.

5.3.2 Light delivery efficiency

The measurement results are summarized in Figure 5.5. As a function of the applied currents ranging from 5 to 25 mA, the light delivery efficiency remained consistent at -10.63 dB. Assuming uniform light output distribution among the fibers, the light delivery efficiency of a single microlens and optical fiber set was expected to be -22.63 dB, which is a moderate level compared to the results reported in existing literature, which are -27.9 to -26.3 dB [33] and -16.3 dB [32]. Note that the values provided here for comparison were recalculated in terms of the measured light intensity results and specification of the optical fiber and LED mentioned in the

works.

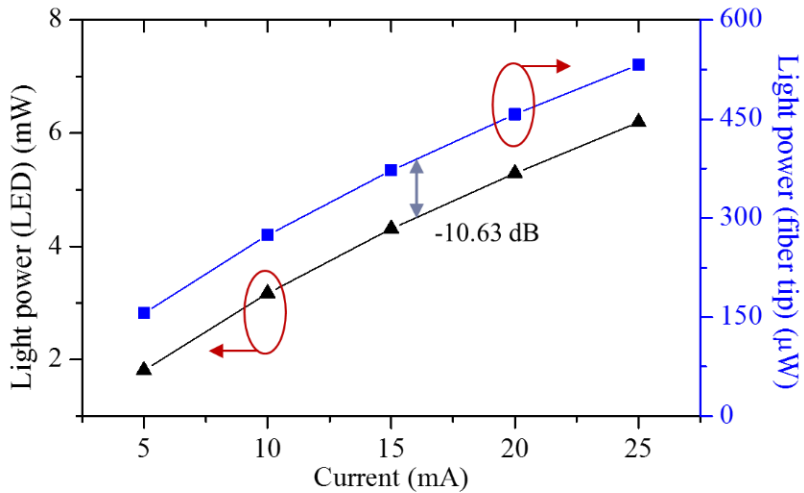


Figure 5.5. Light output power comparison between the LED and the fiber array

Unlike the conventional configuration, the proposed design is advantageous in constructing an array of fibers. Considering that the numerical extension of the fibers directly increases the amount of the delivered light with no additional arrangement of LEDs, the proposed probe is superior in terms of total light power delivery. To put it another way, by adjusting the property and arrangement of the microlenses (for example, enlarging the interval between the fibers and size of the microlens), the proposed probe's light delivery efficiency can be superior even in terms of a single set of microlens and optical fiber due to increased amount of converged light.

The estimated light intensity at the fiber tip is 1.06 mW/mm^2 , which was calculated by dividing the output power by the total area of the fiber core cross-section when the applied current of the LED is 25 mA. The intensity satisfies the

commonly required light level for microbial opsin activation [27, 80]. Moreover, the intensity can be improved by utilizing a different type of LED, as the maximum continuous current rating of the μ LED used in this study is 30 mA.

5.3.3 Loss factor analysis

To examine how much the microlens array directly improves the light delivery efficiency, a sample without the microlens array was separately fabricated for comparison, as illustrated in Figure 5.6. The sample is consisted of a 4×4 optical fiber array assembled to a silicon substrate. The fabrication process of the sample was as follows. A 500 μ m-thick silicon wafer was etched with the same mask used for the fiber guide structure as in Figure 4.6(f), forming 4×4 through-holes penetrating the substrate. Then, the optical fibers manipulated with the same procedure as the neural probe were assembled into the through-holes with the epoxy.

Figure 5.7 shows the comparison of measured light power with and without the microlens array. The light delivery efficiency was improved by 3.15 dB on average. This is relatively low compared to the theoretical expectation, which was 4.41 dB. The dominant cause of efficiency degradation is speculated to be the misalignment of the fiber within the silicon guide structure. Given that the diameter of the silicon guide structure is designed as 250 μ m, a 225 μ m-diameter optical fiber can be placed at a maximum distance of 12.5 μ m from the optical axis.

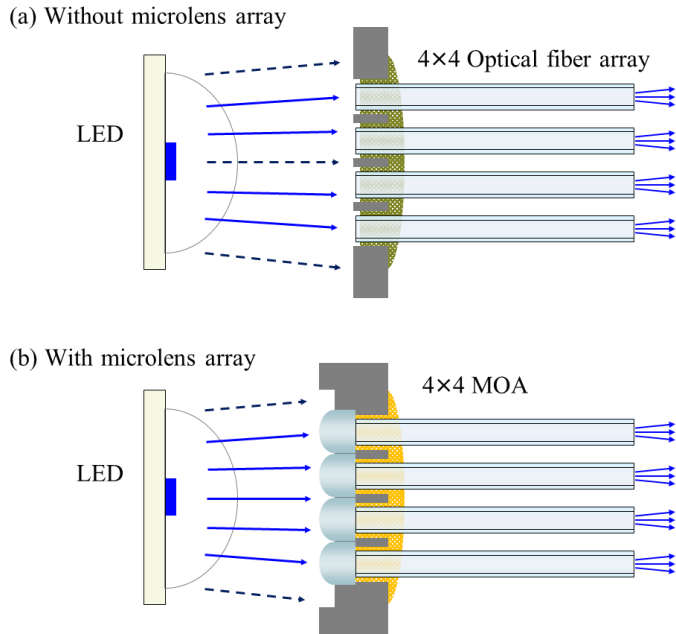


Figure 5.6. Illustration of measurement condition for comparison of the light output power between with and without the microlens

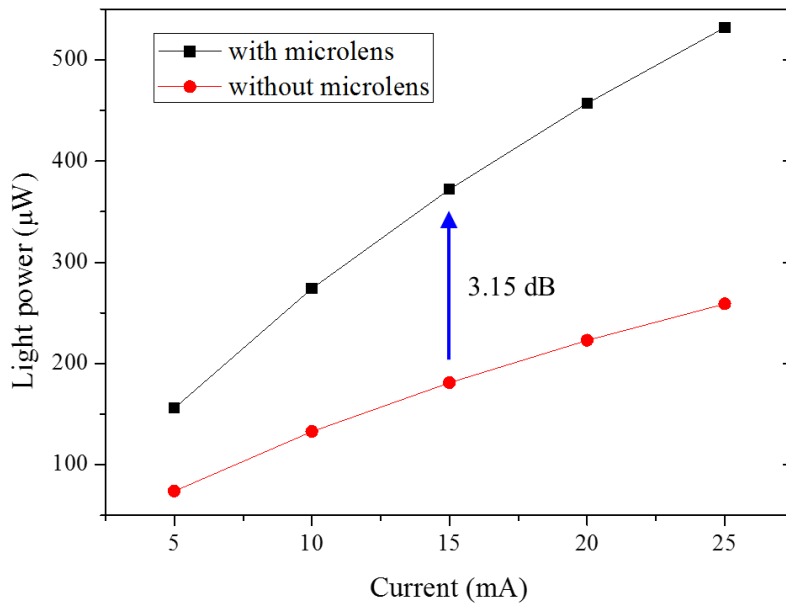


Figure 5.7. Comparison of the measured light power between with and without the

microlens array

To determine the cause and magnitude of the light loss within the neural probe, the practical light power from the LED to the light receiving area of the microlens array was examined. An aperture substrate was separately fabricated for comparison. A 500 μm -thick glass wafer was patterned with Cr using the same mask in Figure 4.6(a), as depicted in Figure 5.8.

Figure 5.9 shows the measurement results. One of the dominant causes of the light delivery efficiency degradation seems to have been the areal mismatch between light receiving area of the microlens array and the effective light emitting area of the LED. Moreover, the practical light emission of the utilized LED, which is assumed as a plane wave, has relatively large dispersive light distribution and light leakage over the given viewing angle.

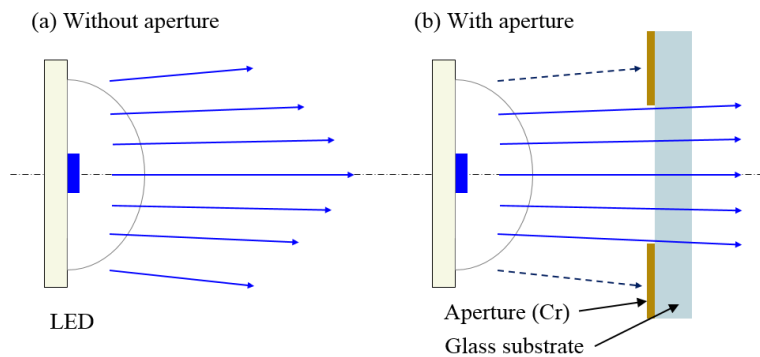


Figure 5.8. Illustration of measurement condition for comparison of the light output power between with and without the aperture

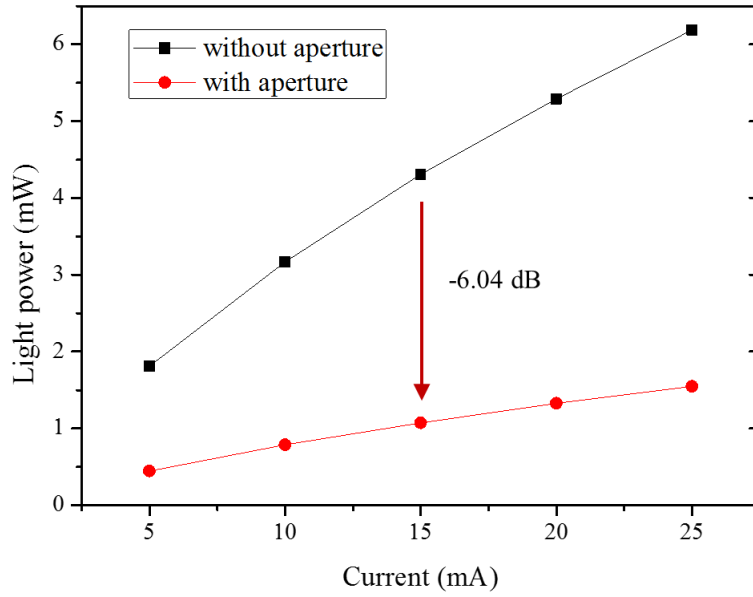


Figure 5.9. Practical light power transmitted to the area of light receiving region of the microlens array

5.4 Capability and limitation

5.4.1 Disposable configuration

The MOA and LED (Figure 5.10(b)) were assembled into disposable and reusable units of customized polycarbonate sheath, respectively (Figure 5.10 (c)). The gap between the MOA and the polycarbonate sheath was sealed with opaque epoxy to prevent possible light or liquid leakage passing through the gap.

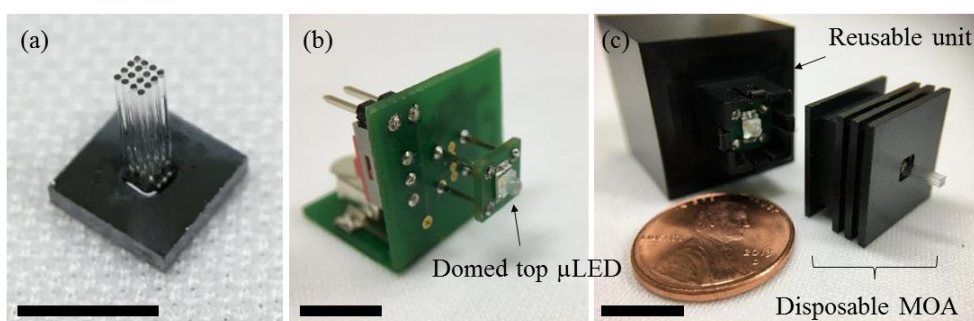


Figure 5.10. Optical images of (a) the fabricated MEMS optrode array, (b) domed-top LED with LED driver, and (c) the overall device including the MEMS optrode array and the reusable unit. The scale bar indicates 5 mm in (a) and 10 mm in (b), (c).

By utilizing the microlens array and fiber guide structure, a separable configuration of the probe between MEMS optrode array and domed-top LED was realized and was successfully verified for its feasibility as a solution to minimizing the wasting part after animal experiment. Nevertheless, a more precise and robust

design of the assembly sheath should be carried out to prevent the degradation of light delivery efficiency caused by the misalignment between the disposable MOA and the reusable LED unit.

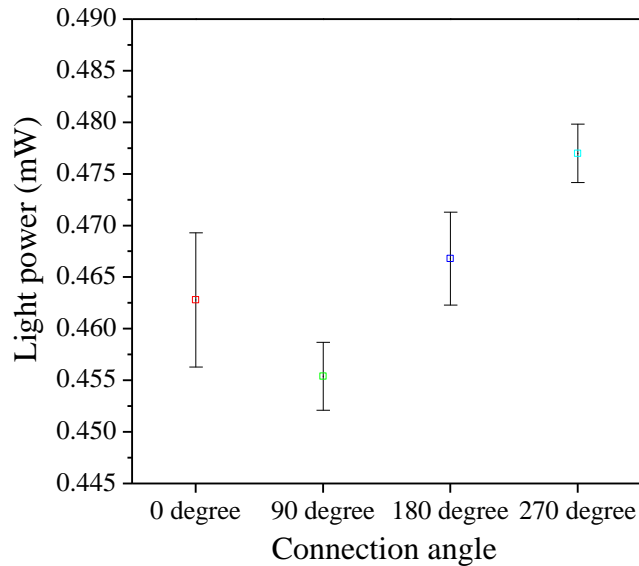


Figure 5.11. Light power measurement

5.4.2 Multi-wavelength illumination

To verify the capability of the multi-wavelength illumination of the probe, the LED was replaced with a multi-wavelength LED and the experiment was repeated, as shown in the optical images (Figure 5.12). One of the great advantages of the proposed device is its structure that enables simple replacement of the light source. An LED (150141YB73100, Würth Electronics, Inc.) capable of illuminating blue

and yellow light were used. The viewing angle of the LED, which is $\pm 60^\circ$, was relatively larger than the previously used blue LED, therefore it was difficult to apply the same design method, which assumes the output light of the LED as collimated beam. However, if a customized LED is used for this probe, it is expected that the design method can be applied as is.

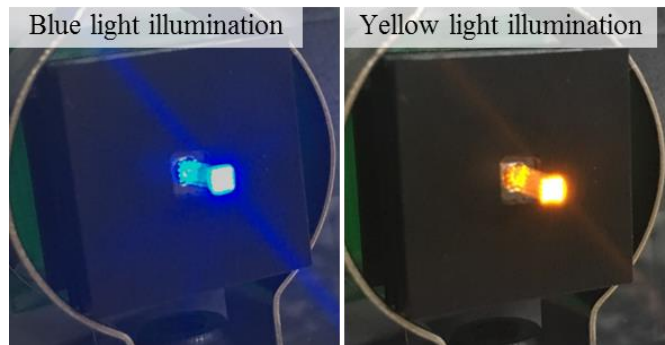


Figure 5.12. Optical image of the multi-wavelength illumination test

To measure the light delivery efficiency at each wavelength, the light output of the LED and probe tip were measured under the same experimental conditions as in *Chapter 5.3.1*. However, in the case of the LED used in the experiment, the blue and yellow diodes were located at a distance from each other within the LED chip, as in most multi-wavelength LEDs. Therefore, precise alignment between the LED and the MOA became more crucial when integrating multi-wavelength LEDs. In the measurement, the light delivery efficiency was measured after aligning the LED and the MOA with the same light delivery efficiency at both wavelengths.

The measured light output powers of the blue and yellow light illumination are summarized in Figure 5.13 and Figure 5.14, respectively. At both wavelengths, the

light delivery efficiency was about -14 dB, which is about half the value of that when using single-wavelength blue LED. Considering the predictable light divergence losses from the large viewing angle characteristics of the LED, these measurements provide a good indication of their capability to integrate with multi-wavelength LEDs.

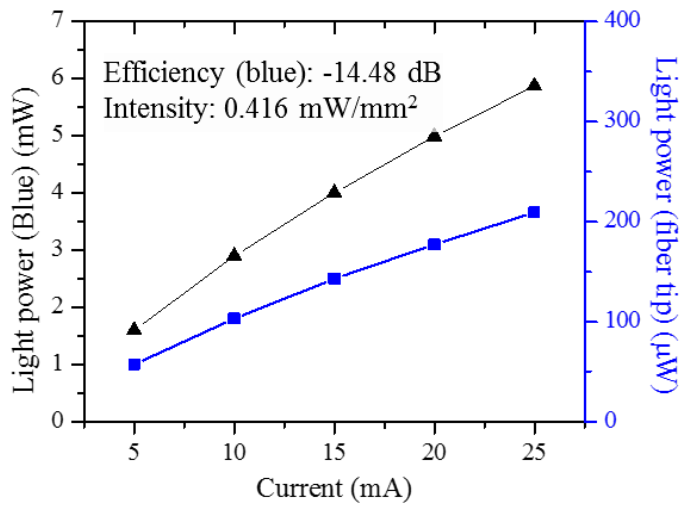


Figure 5.13. Light delivery efficiency of the blue light

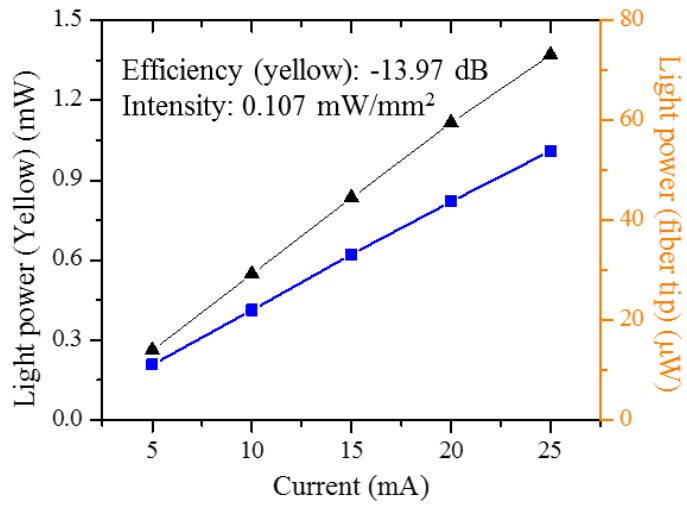


Figure 5.14. Light delivery efficiency of the yellow light

5.5 Conclusion

In this chapter, the fabrication process of the MEMS optrode array including the fiber manipulation and assembly process was described. Several aid structures were presented to improve the completeness of the device. Optical characterization of the MOA was carried out, followed by an analysis on the causes of light loss, which are summarized in Table 5.1. The light loss analysis based on the measurements showed the expected light delivery efficiency from the LED to the probe tip to be -7.87 dB. However, the measured value was -10.63 dB. The dominant cause of this disparity is speculated to be the light scattering loss at the optical fiber facets, which has high roughness due to imprecise cutting by the dicing saw.

Table 5.1. Summary of the measured light delivery efficiency

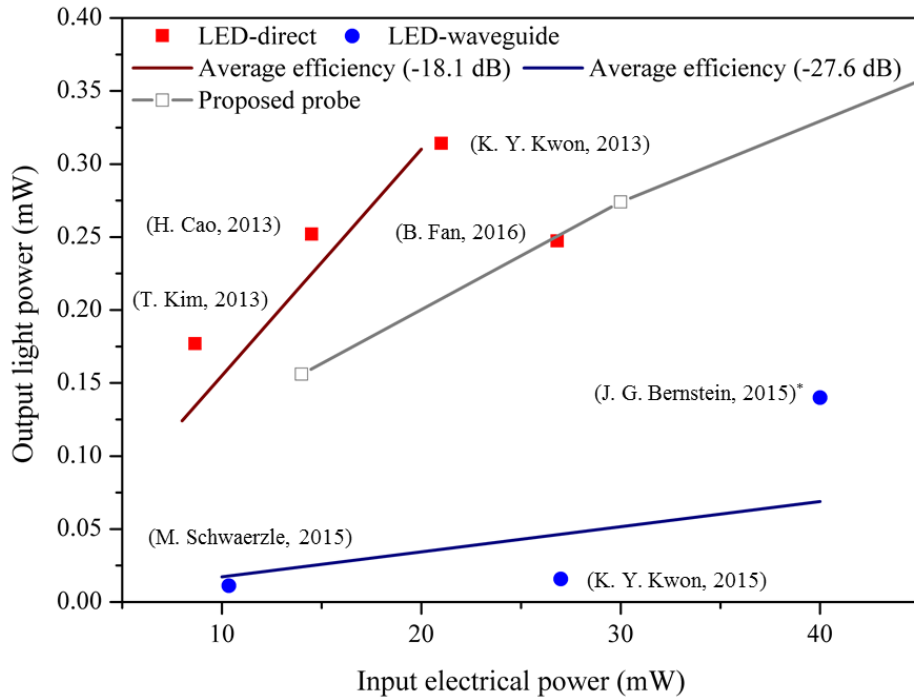
Light loss factors	Design	Expected	Measured
Fresnel reflection	-0.32 dB	-0.32 dB	
Areal mismatch (A_{lens}/A_{LED})	-2.47 dB	-6.04 dB	
MOA ($\eta_{lens-fiber}$)	-0.25 dB	-1.51 dB	
Total	-3.04 dB	-7.87 dB	-10.63 dB

Light delivery efficiency of comparable LED-waveguide-based neural probes are summarized in Table 5.2. The light delivery efficiency of a single set of microlens and optical fiber was calculated to be -22.6 dB based on the measurement. The result is rather moderate compared to other LED-waveguide-based probes. However, the highest total light power, among the conventional LED-waveguide-based optical neural probes, was delivered from a single commercially available LED to the distal tip of the waveguide by expanding the waveguide to an array.

Moreover, it is clear that the proposed device has superior power efficiency. Figure 5.15 compares the proposed device (MOA with the single-wavelength blue LED) with the power efficiency of the conventional devices introduced in *Chapter 1.3.1*. As shown in the figure, the proposed probe showed high power efficiency similar to LED-direct types.

Table 5.2. Light delivery efficiency of LED-waveguide-based neural probes

	MIT (2015)	U Freiburg (2015)	SNU (2017)
Reference	[32]	[33]	This work
Light delivery efficiency (Light output from a single fiber / LED)	-16.3 dB	-25.9 dB	-22.6 dB
Total light delivery efficiency (Total light output / LED)	-16.3 dB	-25.9 dB	-10.6 dB
Power efficiency (Total light output / applied electrical power)	-24.6 dB	-29.7 dB	-20.4 dB



*: Values were scaled down to 1/50 (actual input and output power are 2 W and 7 mW, respectively.)

Figure 5.15. Comparison of power efficiency between the proposed neural probe and conventional LED-based neural probes

6. Conclusion

A new MEMS optrode array (MOA) was developed to improve the light delivery efficiency and functionality. The highest overall optical power was delivered from a single commercially available LED to the tip of the waveguide. To improve light delivery, a novel MEMS microlens array was adopted as an optical collimator between a light source and a waveguide. A simple and practical method for inhibiting surface crystallization in borosilicate glass during high temperature annealing as well as the modeling and fabrication of a through-substrate square-shaped microlens array using a thermal reflow process was proposed and verified, both for the first time in this field of research.

Through the quantitative analysis of the crystallization and from the measured surface ion concentration, no fewer than 30 seconds of fluorine plasma treatments were verified to have significant effectiveness on suppressing the nucleation of cristobalites. A square-shaped glass microlens array was successfully fabricated with good agreement with the design specification. The measurement results fully validated the proposed fabrication procedure and capability of the microlens array as a light collimating optical device in the proposed neural probe.

Light loss analysis based on the measurements showed the expected light delivery efficiency from the LED to probe tip to be -7.87 dB, yet, the measured value was -10.63 dB. Reducing the roughness of the optical fibers' cross-section and designing a more precise assembly sheath will improve the light delivery efficiency.

This study proposed and validated a new neural probe to improve the low optical power handling issues, including low light delivery efficiency and low light output power, of conventional devices. In addition to optogenetics, it is expected for the proposed device and its design and fabrication method to be applied to diverse applications in integrated optical fibers and optical MEMS devices.

Bibliography

- [1] Deisseroth K, Feng G P, Majewska A K, Miesenbock G, Ting A and Schnitzer M J 2006 Next-generation optical technologies for illuminating genetically targeted brain circuits *J Neurosci* **26** (41) 10380-6
- [2] Deisseroth K 2011 Optogenetics *Nat Methods* **8** (1) 26-9 Epub 2010/12/31
- [3] Zemelman B V, Lee G A, Ng M and Miesenbock G 2002 Selective photostimulation of genetically ChARGed neurons *Neuron* **33** (1) 15-22
- [4] Hunter P 2016 Shining a light on optogenetics: Advances in electronics and protein engineering advance the field of optogenetics to study the activity of neuronal networks *Embo Rep* **17** (5) 634-7
- [5] Deisseroth K 2010 Controlling the Brain with Light *Sci Am* **303** (5) 48-55
- [6] Deisseroth K 2015 Optogenetics: 10 years of microbial opsins in neuroscience *Nat Neurosci* **18** (9) 1213-25
- [7] Warden M R, Cardin J A and Deisseroth K 2014 Optical neural interfaces *Annu Rev Biomed Eng* **16** 103-29 Epub 2014/07/12
- [8] Adamantidis A R, Zhang F, Aravanis A M, Deisseroth K and De Lecea L 2007 Neural substrates of awakening probed with optogenetic control of hypocretin neurons *Nature* **450** (7168) 420-U9
- [9] Aravanis A M, Wang L P, Zhang F, Meltzer L A, Mogri M Z, Schneider M B and Deisseroth K 2007 An optical neural interface: in vivo control of rodent motor cortex with integrated fiberoptic and optogenetic technology *J Neural Eng* **4** (3) S143-S56
- [10] Stark E, Koos T and Buzsaki G 2012 Diode probes for spatiotemporal optical

- control of multiple neurons in freely moving animals *J Neurophysiol* **108** (1) 349-63
- [11] Chen S Y, Pei W H, Gui Q, Chen Y F, Zhao S S, Wang H and Chen H D 2013 A fiber-based implantable multi-optrode array with contiguous optical and electrical sites *J Neural Eng* **10** (4)
- [12] Wu F, Stark E, Im M, Cho I J, Yoon E S, Buzsaki G, Wise K D and Yoon E 2013 An implantable neural probe with monolithically integrated dielectric waveguide and recording electrodes for optogenetics applications *J Neural Eng* **10** (5)
- [13] Rubehn B, Wolff S B E, Tovote P, Luthi A and Stieglitz T 2013 A polymer-based neural microimplant for optogenetic applications: design and first in vivo study *Lab Chip* **13** (4) 579-88
- [14] Abaya T V, Blair S, Tathireddy P, Rieth L and Solzbacher F 2012 A 3D glass optrode array for optical neural stimulation *Biomed Opt Express* **3** (12) 3087-104 Epub 2012/12/18
- [15] Kim T I *et al.* 2013 Injectable, Cellular-Scale Optoelectronics with Applications for Wireless Optogenetics *Science* **340** (6129) 211-6
- [16] Cao H, Gu L, Mohanty S K and Chiao J C 2013 An Integrated mu LED Optrode for Optogenetic Stimulation and Electrical Recording *Ieee T Bio-Med Eng* **60** (1) 225-9
- [17] Kwon K Y, Sirowatka B, Weber A and Li W 2013 Opto-mu ECoG Array: A Hybrid Neural Interface With Transparent mu ECoG Electrode Array and Integrated LEDs for Optogenetics *Ieee T Biomed Circ S* **7** (5) 593-600
- [18] Fan B, Kwon K Y, Weber A and Li W. An implantable, miniaturized SU-8 optical probe for optogenetics-based deep brain stimulation. *Engineering in Medicine and Biology Society (EMBC), 2014 36th Annual International*

Conference of the IEEE2014.

- [19] Kwon K Y, Lee H M, Ghovanloo M, Weber A and Li W 2015 Design, fabrication, and packaging of an integrated, wirelessly-powered optrode array for optogenetics application *Frontiers in systems neuroscience* **9**
- [20] Fan B, Kwon K Y, Rechenberg R, Becker M F, Weber A J and Li W 2016 A hybrid neural interface optrode with a polycrystalline diamond heat spreader for optogenetics *Technology* **4** (1) 15-22
- [21] Zorzos A N, Scholvin J, Boyden E S and Fonstad C G 2012 Three-dimensional multiwaveguide probe array for light delivery to distributed brain circuits *Opt Lett* **37** (23) 4841-3 Epub 2012/12/04
- [22] Fan B and Li W 2015 Miniaturized optogenetic neural implants: a review *Lab Chip* **15** (19) 3838-55 Epub 2015/08/27
- [23] McCall J G, Kim T I, Shin G, Huang X, Jung Y H, Al-Hasani R, Omenetto F G, Bruchas M R and Rogers J A 2013 Fabrication and application of flexible, multimodal light-emitting devices for wireless optogenetics *Nat Protoc* **8** (12) 2413-28
- [24] Lee S T, Williams P A, Braine C E, Lin D T, John S W M and Irazoqui P P 2015 A Miniature, Fiber-Coupled, Wireless, Deep-Brain Optogenetic Stimulator *Ieee T Neur Sys Reh* **23** (4) 655-64
- [25] Iwai Y, Honda S, Ozeki H, Hashimoto M and Hirase H 2011 A simple head-mountable LED device for chronic stimulation of optogenetic molecules in freely moving mice *Neurosci Res* **70** (1) 124-7
- [26] Wentz C T, Bernstein J G, Monahan P, Guerra A, Rodriguez A and Boyden E S 2011 A wirelessly powered and controlled device for optical neural control of freely-behaving animals *J Neural Eng* **8** (4)
- [27] Boyden E S, Zhang F, Bamberg E, Nagel G and Deisseroth K 2005

Millisecond-timescale, genetically targeted optical control of neural activity
Nat Neurosci **8** (9) 1263-8

- [28] Zhang F *et al.* 2007 Multimodal fast optical interrogation of neural circuitry
Nature **446** (7136) 633-U4
- [29] Gradinaru V, Zhang F, Ramakrishnan C, Mattis J, Prakash R, Diester I, Goshen I, Thompson K R and Deisseroth K 2010 Molecular and Cellular Approaches for Diversifying and Extending Optogenetics *Cell* **141** (1) 154-65
- [30] Yizhar O, Fenno L E, Davidson T J, Mogri M and Deisseroth K 2011 Optogenetics in Neural Systems *Neuron* **71** (1) 9-34
- [31] Tye K M *et al.* 2013 Dopamine neurons modulate neural encoding and expression of depression-related behaviour *Nature* **493** (7433) 537-+
- [32] Bernstein J G, Allen B D, Guerra A A and Boyden E S 2015 Processes for design, construction and utilisation of arrays of light-emitting diodes and light-emitting diode-coupled optical fibres for multi-site brain light delivery *The Journal of Engineering* **1** (1)
- [33] Schwaerzle M, Elmlinger P, Paul O and Ruther P. Miniaturized 3× 3 optical fiber array for optogenetics with integrated 460 nm light sources and flexible electrical interconnection. *Micro Electro Mechanical Systems (MEMS), 2015 28th IEEE International Conference on 18-22 January; Estoril2015.* p. 162 - 5.
- [34] Hudson M C 1974 Calculation of Maximum Optical Coupling Efficiency into Multimode Optical-Waveguides *Appl Optics* **13** (5) 1029-33
- [35] Abaya T V F, Diwekar M, Blair S, Tathireddy P, Rieth L and Solzbacher F 2014 Deep-tissue light delivery via optrode arrays *J Biomed Opt* **19** (1)
- [36] Kawasaki B S and Johnson D C 1975 Bulb-Ended Fiber Coupling to Led Sources *Opt Quant Electron* **7** (4) 281-8

- [37] Gabardi D R and Shealy D L 1986 Coupling of Domed Light-Emitting-Diodes with a Multimode Step-Index Optical Fiber *Appl Optics* **25** (19) 3435-42
- [38] https://en.wikipedia.org/wiki/Refractive_index. accessed 31 JAN 2017
- [39] <http://www.schott.com/borofloat/english/download/>. accessed 31 March 2014
- [40] <https://www.thorlabs.com/thorproduct.cfm?partnumber=FP200URT>. accessed 31 JAN 2017
- [41] http://www.epotek.com/site/administrator/components/com_products/. accessed 31 JAN 2017
- [42] Tuchin V V. Handbook of Optical Biomedical Diagnostics: SPIE Press; 2002 15 April.
- [43] Yoo S, Jin J Y, Ha J G, Ji C H and Kim Y K 2014 Two-dimensional optical scanner with monolithically integrated glass microlens *Journal of Micromechanics and Microengineering* **24** (5)
- [44] He M, Yuan X C, Moh K J, Bu J and Yi X J 2004 Monolithically integrated refractive microlens array to improve imaging quality of an infrared focal plane array *Opt Eng* **43** (11) 2589-94
- [45] Kim S M, Choi M, Kim H, Lim J and Kang S 2008 Development of method to model surface of reflowed square microlens for image sensor *Electronics Letters* **44** (7) 492-U10
- [46] Jin J Y, Yoo S, Yoo B W and Kim Y K 2012 Characterisation of silicon through-vias for wafer-level interconnection with glass reflows *Electronics Letters* **48** (21) 1354-5
- [47] Lee J Y, Lee S W, Lee S K and Park J H 2013 Through-glass copper via using the glass reflow and seedless electroplating processes for wafer-level RF MEMS packaging *Journal of Micromechanics and Microengineering* **23** (8)

- [48] Lee Y-T, Lin C-W, Lin C-M, Yeh S-R, Chang Y-C and Fang W 2010 A pseudo 3D glass microprobe array: glass microprobe with embedded silicon for alignment and electrical interconnection during assembly *Journal of Micromechanics and Microengineering* **20** (2) 025014
- [49] Kim J K and Baek C W 2013 Capacitive pressure sensor with wafer-through silicon vias using SOI-Si direct wafer bonding and glass reflow technique *Ieice Electron Expr* **10** (15)
- [50] Chen Y, Yi A Y, Yao D, Klocke F and Pongs G 2008 A reflow process for glass microlens array fabrication by use of precision compression molding *Journal of Micromechanics and Microengineering* **18** (5) 055022
- [51] Yoo S, Jin J Y, Ha J G, Ji C H and Kim Y K. 2-D Forward Optical Scanner with Glass Microlens and Isolation Blocks Using Thermal Reflow. 2012 *International Conference on Optical MEMS and Nanophotonics*; Banff, Canada2012.
- [52] Yoo S, Ha J G, Jin J Y, Ji C H and Kim Y K 2013 Monolithically integrated glass microlens scanner using a thermal reflow process *Journal of Micromechanics and Microengineering* **23** (6)
- [53] Marotta A, Buri A and Branda F 1980 Surface and Bulk Crystallization in Non-Isothermal Devitrification of Glasses *Thermochimica Acta* **40** (3) 397-403
- [54] Mogulkoc B, Jansen H V, Berenschot J W, ter Brake H J M, Knowles K M and Elwenspoek M C 2009 Characterization of MEMS-on-tube assembly: reflow bonding of borosilicate glass (Duran (R)) tubes to silicon substrates *Journal of Micromechanics and Microengineering* **19** (8)
- [55] Mogulkoc B, Knowles K M, Jansen H V, ter Brake H J M and Elwenspoek M C 2010 Surface Devitrification and the Growth of Cristobalite in Borofloat (R) (Borosilicate 8330) Glass *J Am Ceram Soc* **93** (9) 2713-9

- [56] Marler B 1988 On the Relationship between Refractive-Index and Density for SiO₂-Polymorphs *Phys Chem Miner* **16** (3) 286-90
- [57] Hoshino T and Nishioka Y 1999 Etching process of SiO₂ by HF molecules *J Chem Phys* **111** (5) 2109-14
- [58] Jean J H and Gupta T K 1993 Alumina as a Devitrification Inhibitor during Sintering of Borosilicate Glass Powders *J Am Ceram Soc* **76** (8) 2010-6
- [59] Jean J H, Chang C R, Kuan T H and Lin C H 1995 Suppression of Crystallization during Sintering of Lead Borosilicate Glass Powders *Mater Chem Phys* **42** (1) 56-61
- [60] Lima M M and Monteiro R 2001 Characterisation and thermal behavior of a borosilicate glass *Thermochimica Acta* **6**
- [61] Leech P W 1999 Reactive ion etching of quartz and silica-based glasses in CF₄/CHF₃ plasmas *Vacuum* **55** (3-4) 191-6
- [62] Metwalli E and Pantano C G 2003 Reactive ion etching of glasses: Composition dependence *Nucl Instrum Meth B* **207** (1) 21-7
- [63] Aguirre A D, Herz P R, Chen Y, Fujimoto J G, Piyawattanametha W, Fan L and Wu M C 2007 Two-axis MEMS scanning catheter for ultrahigh resolution three-dimensional and en face imaging *Optics Express* **15** (5) 2445-53
- [64] Mu X J, Sun W, Feng H H, Yu A B, Chen K W S, Fu C Y and Olivo M 2011 MEMS micromirror integrated endoscopic probe for optical coherence tomography bioimaging *Sensor Actuat a-Phys* **168** (1) 202-12
- [65] Jin J Y, Park J H, Yoo B W, Jang Y H and Kim Y K 2011 Numerical analysis and demonstration of a 2-DOF large-size micromirror with sloped electrodes *Journal of Micromechanics and Microengineering* **21** (9)
- [66] Kwon S and Lee L P 2002 Stacked two Dimensional Micro-lens Scanner for

- Micro Confocal Imaging Array Proc. *the 15th IEEE International Conference on MEMS* (Las Vegas, USA) pp 483-6
- [67] Chiao M, Siu C P B and Zeng H 2007 Magnetically actuated MEMS microlens scanner for in vivo medical imaging *Optics Express* **15** (18) 11154-66
- [68] Park H C, Song C and Jeong K H 2010 Micromachined lens microstages for two-dimensional forward optical scanning *Optics Express* **18** (15) 16133-8
- [69] Choi W, Sigal G, Rubtsov V and Kim C-J 2012 A micro translating lens unit for stereo imaging through single-image endoscope Proc. *the 25th IEEE International Conference on MEMS* (Paris, France) pp 3-6
- [70] Quack N, Chou J B and Wu M C 2012 Self-aligned VCSEL-microlens scanner with large scan range Proc. *the 25th IEEE International Conference on MEMS* (Paris, France) pp 656-9
- [71] Choo H and Muller R S 2006 Addressable microlens array to improve dynamic range of Shack-Hartmann sensors *J Microelectromech S* **15** (6) 1555-67
- [72] Chou J, Yu K, Horsley D, Yoxall B, Mathai S, Tan M R T, Wang S Y and Wu M C 2009 Robust free space board-to-board optical interconnect with closed loop MEMS tracking *Appl Phys a-Mater* **95** (4) 973-82
- [73] Merz P, Quenzer H J, Bernt H, Wagner B and Zoberbier M 2003 A novel micromachining technology for structuring borosilicate glass substrates Proc. *The 12th International Conference on Solid State Sensors, Actuators and Microsystems* (Boston, US) pp 258-61
- [74] Lee D-W, Oh J-K, Choi J-S, Lee H-J and Chung W-N 2010 Wafer-level Fabrication of Ball Lens by Cross-cut and Reflow of Wafer-bonded Glass on Silicon *Journal of the Optical Society of Korea* **14** (2) 163-9
- [75] Lee S-K, Kim M-G, Jo K-W, Shin S-M and Lee J-H 2008 A glass reflowed

microlens array on a Si substrate with rectangular through-holes *Journal of Optics A: Pure and Applied Optics* **10** (4) 044003

- [76] Nieto D, Arines J, Gomez-Reino C, O'Connor G M and Flores-Arias M T 2011 Fabrication and characterization of microlens arrays on soda-lime glass using a combination of laser direct-write and thermal reflow techniques *J Appl Phys* **110** (2)
- [77] Firestone G C and Yi A Y 2005 Precision compression molding of glass microlenses and microlens arrays - an experimental study *Appl Optics* **44** (29) 6115-22
- [78] Daly D, Stevens R F, Hutley M C and Davies N 1990 The Manufacture of Microlenses by Melting Photoresist *Meas Sci Technol* **1** (8) 759-66
- [79] Yoo S, Ji C H, Jin J Y and Kim Y K 2014 Suppression of surface crystallization on borosilicate glass using RF plasma treatment *Appl Surf Sci* **316** 484-90
- [80] Chow B Y *et al.* 2010 High-performance genetically targetable optical neural silencing by light-driven proton pumps *Nature* **463** (7277) 98-102

Abstract (Korean)

본 논문은 향상된 광 전달 효율과 다파장 광 자극 능력을 갖춘 MEMS 광 탐침 어레이(MEMS optrode array, MOA)를 기반으로 하는 광학 신경 프로브에 관한 연구이다. 제안된 시스템은 도파로를 어레이로 확장함으로써 기존에 보고된 LED 도파관 기반의 광 신경 프로브 중에서 가장 높은 광력을 단일 LED로부터 프로브 출력단으로 전달하였다. 광 전달을 향상시키기 위하여 MEMS 마이크로렌즈 어레이를 처음 적용하였다. 또한, 붕규산 유리를 이용한 열 용융 공정에서 발생하는 치명적인 문제인 표면 결정화를 억제하는 간단하고 실용적인 방법을 처음으로 제안하고 검증하였다. 이를 기반으로 열 용융 공정을 이용한 기관 관통형 사각 유리 마이크로렌즈 어레이의 모델링 및 제작하였다.

제안된 프로브는 일회용 MOA 부분과 재사용 가능 부분으로 구성된다. MOA는 4×4 어레이의 6 mm 길이 광섬유 및 사각 유리 마이크로렌즈로 구성되며, 재사용 가능 부분은 상부 돔형 LED (Domed-top LED) 및 구동 회로로 구성된다. 일회용 MOA는 동물 실험 후 전체 프로브에서 낭비되는 부분을 최소화는 동시에 프로브 재사용으로 인한 감염 위험성을 감소시킨다. 마이크로렌즈의 형상은 전산 유체 역학 및 기하 광학에 기반을 둔 유한 요소 해석을 통해 최적화하였다.

붕규산 유리의 표면 결정화는 열 용융 공정 전 간단한 표면 처리를 통해 억제하였다. 유리 표면 이온 농도와 결정화 정도의 상관관계를

정량적으로 분석하여 30 초 이상의 플루오르화물 플라즈마 처리가 크리스토팔라이트의 핵형성을 억제하는 데 상당한 효과가 있음이 입증하였다. 이를 통해 평균 표면 거칠기를 15배, 광학적 투명도를 3배 향상시켰다. 밀면적 $300 \times 300 \mu\text{m}^2$ 인 사각 유리 마이크로렌즈는 유한 분석 모델링과 잘 일치되고 균일하게 제작되었다. 유리 표면 결정화는 효과적으로 억제되었으며 47 nm의 평균 표면 거칠기를 달성하였다. 광섬유의 분절 및 조립은 맞춤형 보조 장치를 사용하여 이루어졌다.

제안된 프로브의 광 전달 효율은 별도로 제작된 세 가지 대조군과 그 특성을 비교하여 면밀하게 분석되었다. 프로브의 총 광 전달 효율은 -10.63 dB로 측정되었으며 마이크로렌즈 적용으로 인한 효율 향상은 3.15 dB로 측정되었다. 광 전달 효율 저하의 주된 원인은 LED와 마이크로렌즈 사이의 낮은 결합 효율(-6.04 dB)과, 다이싱된 광섬유의 거친 단면에서 기인하였다. 프로브의 광원을 다파장 LED로 교체하여 다파장 광 자극의 가능성 또한 성공적으로 검증하였으며 각 파장에서의 광 전달 효율은 모두 약 -14 dB로 측정되었다.